Grain Alignment in the Circumstellar Shell of IRC+10° 216

B-G Andersson[1] , Enrique Lopez-Rodriguez[1,2] , Ilija Medan[3] , Archana Soam[1,4] , Thiem Hoang[5] , John E. Vaillancourt[6] ,
Alex Lazarian[7,8] , Christer Sandin[9] , Lars Mattsson[9] , and Mehrnoosh Tahani[10]

[1] SOFIA Science Center, Universities Space Research Association, NASA Ames Research Center, M.S. N232-12, Moffett Field, CA 94035, USA
[2] Kavli Institute for Particle Astrophysics & Cosmology (KIPAC), Stanford University, Stanford, CA 94305, USA
[3] Department of Physics and Astronomy, Georgia State University, Atlanta, GA 30302, USA
[4] Indian Institute of Astrophysics, II Block, Koramangala, Bengaluru 560034, India
[5] Korea Astronomy and Space Science Institute, Daejeon 34055, Republic of Korea; Korea University of Science and Technology, 217 Gajeong-ro, Yuseong-gu,
Daejeon, 34113, Republic of Korea
[6] Lincoln Laboratory, Massachusetts Institute of Technology, 244 Wood St., Lexington, MA 02421, USA
[7] Department of Astronomy, University of Wisconsin, 475 North Charter Street, Madison, WI 53706, USA
[8] Centro de Investigación en Astronomía, Universidad Bernardo O'Higgins, Santiago, General Gana 1760, 8370993, Chile
[9] Nordita, KTH Royal Institute of Technology and Stockholm University, Roslagstullsbacken 23, SE-106 91 Stockholm, Sweden
[10] Dominion Radio Astrophysical Observatory, Herzberg Astronomy and Astrophysics Research Centre, National Research Council Canada, P.O. Box 248, Penticton,
BC, V2A 6J9, Canada

Abstract

Dust-induced polarization in the interstellar medium (ISM) is due to asymmetric grains aligned with an external reference direction, usually the magnetic field. For both the leading alignment theories, the alignment of the grain's angular momentum with one of its principal axes and the coupling with the magnetic field requires the grain to be paramagnetic. Of the two main components of interstellar dust, silicates are paramagnetic, while carbon dust is diamagnetic. Hence, carbon grains are not expected to align in the ISM. To probe the physics of carbon grain alignment, we have acquired Stratospheric Observatory for Infrared Astronomy/Higch-resolution Airborne Wideband Camera-plus far-infrared photometry and polarimetry of the carbon-rich circumstellar envelope (CSE) of the asymptotic giant branch star IRC+10° 216. The dust in such CSEs are fully carbonaceous and thus provide unique laboratories for probing carbon grain alignment. We find a centrosymmetric, radial, polarization pattern, where the polarization fraction is well correlated with the dust temperature. Together with estimates of a low fractional polarization from optical polarization of background stars, we interpret these results to be due to a second-order, direct radiative external alignment of grains without internal alignment. Our results indicate that (pure) carbon dust does not contribute significantly to the observed ISM polarization, consistent with the nondetection of polarization in the 3.4 μm feature due to aliphatic CH bonds on the grain surface.

Unified Astronomy Thesaurus concepts: Circumstellar dust (236); Magnetic fields (994); Carbonaceous grains (201); Asymptotic giant branch stars (2100)

1. Introduction

Interstellar polarization was first discovered at optical wavelengths in 1949 (Hall 1949; Hiltner 1949b) and was almost immediately identified to be due to dichroic extinction by asymmetric dust grains aligned with the interstellar magnetic field (Hiltner 1949a). The complementary polarized infrared thermal emission was subsequently detected in 1982 (Cudlip et al. 1982). Because of the broad wavelength span of this polarization from the ultraviolet (UV) to submillimeter wavelengths, and its relative ease of observation, such dust-induced polarization provides an important probe of the interstellar magnetic field structure and strength (Davis 1951; Chandrasekhar & Fermi 1953; Houde et al. 2009).

While the general association of polarization with aligned dust grains and the magnetic field has been well established (e.g., Whittet 2003), the physical mechanism responsible for the grain alignment long remained unclear. To reliably interpret polarization observations, a fully developed, well-tested theory of grain alignment is required.

Generally, for significant polarization to be produced two forms of grain alignment must occur: "internal" and "external." *Internal alignment* refers to the process of aligning each grain's angular momentum with one of its principal axes, while *external alignment* refers to the process of aligning the grain angular momentum along a common reference direction. Internal alignment ensures a time-constant dichroic extinction (or emission) for a given grain and observation direction.

For a nonspherical grain under conservation of angular momentum, the lowest energy state occurs when the angular momentum is aligned with the axis of maximum moment of inertia (i.e., the short grain axis). As discussed by Purcell (1979), to align the grain from its initial arbitrary rotation orientation to this equilibrium state requires energy dissipation, through either inelastic deformations (Lazarian & Efroimsky 1999) or through electronic Barnett relaxation, of which the latter was found to dominate by Purcell (1979). Those results were confirmed and extended to include nuclear spins by Lazarian & Draine (1999a).

1.1. Grain Alignment Mechanisms

1.1.1. Davis–Greenstein Alignment

Several mechanisms have been proposed for the external alignment. The long-standing theory by Davis & Greenstein (1951)

relies on paramagnetic relaxation in a rapidly rotating dust grain, and requires a temperature difference between the gas and the dust (Jones & Spitzer 1967). Theoretical considerations in the 1990s regarding the coupling of grain rotation and internal excitations (e.g., phonons; Lazarian & Draine 1999b), and observations of grain alignment at large opacities into molecular clouds (Jones et al. 1984; Hough et al. 2008), as well as the lack of a correlation between the amount of ferromagnetic material in the grains and the amount of observed polarization (Voshchinnikov et al. 2012), put this mechanism is serious doubt, at least for the "classical" large grains (see Hoang et al. 2014).

1.1.2. Radiative Alignment

An alternative theoretical paradigm, based on radiative torques, was introduced by Dolginov & Mitrofanov (1976), clarified through numerical studies (Draine & Weingartner 1996), and eventually formulated as an analytical theory of grain alignment (Lazarian & Hoang 2007a). This radiative alignment torque (RAT) theory has now been extensively tested and, to date, supported by observations (Andersson et al. 2015).

RAT alignment (Lazarian & Hoang 2007a) occurs when an irregular grain is spun up by the net torque induced by the difference in scattering efficiency of the right- and left-hand circularly polarized components of an anisotropic illuminating radiation field. This spin-up has been confirmed by laboratory studies (Abbas et al. 2006). For a rotating paramagnetic grain, the total energy can be lowered, while conserving angular momentum, by transferring some of the angular momentum from the bulk rotation to internal quantum spin flips. This is known as the Barnett effect, and is the inverse of the experimentally well-established Einstein–de Haas effect (Richardson 1908; Einstein & de Haas 1915). A grain which does not rotate around one of its axes of symmetry will nutate, and the Barnett effect will then be time variable in the grain bulk. With a fast nutation the Barnett effect will become dissipative (Purcell 1979), leading to internal grain alignment (whence the grain is rotating around one of its axes of symmetry).

In equilibrium, the Barnett effect balances the grain rotation with an asymmetry in the quantum spin distribution. Because quantum spins carry both angular and magnetic momenta, such a rearrangement of the spin distribution will impart a net magnetization to the grain. This magnetization then couples to an external magnetic field, causing the grain's angular momentum vector to Larmor precess around the field lines. The continued radiative torques on the grain over the Larmor precession process eventually aligns the angular momentum of the grain with the magnetic field direction (Lazarian & Hoang 2007a).

Therefore, in both Davis–Greenstein (DG) and RAT alignment, the external alignment is accomplished through the interaction of the external magnetic field with a paramagnetic bulk solid in a rotating dust grain.

For a strong, anisotropic radiation field, RAT theory predicts that the alignment reference axis can change from the magnetic field ("B-RAT") to the propagation direction (k-vector) of the radiation field ("k-RAT"; Lazarian & Hoang 2007a). For grains with efficient internal alignment the position angle of dichroic extinction polarization will then follow the radiation field direction. This means that if a grain is internally aligned and located close to a strong radiation source, we would expect to observe emission-polarization perpendicular to the direction from the radiation source. This effect has been claimed in protostellar disks (Kataoka et al. 2017) and possibly in the Orion Bar (Chuss et al. 2019) and OMC-1 (Pattle et al. 2021). For grains with slow (or no) internal alignment, k-RAT alignment is still possible, albeit inefficient. As shown by Hoang & Lazarian (2009), the dynamics of such grains will exhibit several weak attractor points, with the axis of maximum inertia oriented either parallel or perpendicular to the radiation field (see Hoang & Lazarian 2009, Figure 19).

1.1.3. Mechanical Alignment

In addition to DG and the various RAT mechanisms, mechanical alignment (i.e., Gold alignment; Gold 1952) may also be the cause of the observed polarization. To achieve mechanical alignment an anisotropic, supersonic, gas–dust drift velocity must be set up (for subsonic flows isotropic sound waves will significantly lessen—or eradicate—any net alignment). Gold alignment and its modifications (see Lazarian 1994, 1995a) as well as the cross-section mechanical alignment introduced in Lazarian (1995b; see, also, Lazarian & Efroimsky 1996; Lazarian et al. 1996) act to align the grains with long axes along the flow.

While the balancing effects of disalignment mechanisms (e.g., Draine & Lazarian 1998) is always an important consideration for the absolute alignment efficiency. it is crucial for mechanical alignment as collisions here drive both the alignment and disalignment. As discussed for alignment in shocks by Hoang & Lee (2020; see Section 5.2), for a supersonic drift velocity the alignment is independent of the gas density.

A new mechanism of collisionally induced alignment of irregular grains was introduced in Lazarian & Hoang (2007b). This mechanical torque (MET) alignment mechanism acts similar to the RAT mechanism, replacing the scattering of photons with the scattering of particles off of the helical surface of the grain, and aligning the grains with long axes perpendicular to the relative grain–gas motion.

The MET mechanism was recently tested numerically (Hoang et al. 2018) and was shown to be more efficient than the earlier introduced mechanical alignments, such as Gold alignment. Therefore, from theory and numerical simulations we expect the gaseous flow, as a primary alignment force, will align grains with internal alignment with their large axis perpendicular to the direction of the flow.

Hoang & Lazarian (2009) performed extensive calculations of RAT alignment, with and without internal relaxation, and found that for a 0.1 μm grain, and a radiation field 100 times the interstellar one, the RAT alignment time is more than an order of magnitude faster than that for mechanical alignment.

1.1.4. Electrical Alignment

Another possibility for carbon grain alignment was recently proposed by Lazarian (2020) employing the precession of an electrically charged grain in a magnetic field. Because asymptotic giant branch (AGB) circumstellar envelopes (CSEs) are expected to have low ionization levels, and the work functions for both amorphous carbon and SiC are relatively high, 4–6 eV (Liu et al. 2019) and ~4.8 eV (Pelletier et al. 1984), respectively, few photoelectrons are going to be available in the inner part of the CSE. As shown by Mauron & Huggins (2010), even at the location of "Star 6",

37″ from CW Leo, most elemental species are predominantly in their neutral state, including K I (ionization potential: 4.3 eV). Hence it is unlikely that the dust grains are significantly charged in the dense part of the CSE probed by our observations. We will, therefore, not consider this mechanism here.

1.2. Grain Alignment in Asymptotic Giant Branch Envelopes

The outflows in AGB stars are driven by radiation pressure on dust grains, which drags the gas along through collisional coupling (e.g., Gail & Sedlmayr 2013). As material expands in a spherical outflow, the gas and dust phases decouple, already close to where dust first forms at a few stellar radii, and a significant gas–dust drift velocity is established (Section 4.3; Sandin & Mattsson 2020). Such a drift would provide the supersonic gas–dust velocities required for mechanical alignment. Because of mass conservation, in an outflow with constant expansion velocity a density profile of $n \propto 1/r^2$ is set up. The radiation from the central star provides the strong anisotropic radiation field required for the various RAT mechanisms.

In an AGB envelope, B-RAT alignment should give rise to a polarization pattern following the projection of the star's magnetic field, as seen in the oxygen-rich CSE of IK Tau (B.-G. Andersson et al. 2022, in preparation), or, if the outflow energy dominates the magnetic field, an azimuthal polarization geometry. First-order k-RAT (for grains with efficient internal alignment) should also produce an azimuthal emission-polarization pattern, as would grains aligned with the MET mechanism. For mechanical, e.g., Gold, alignment we would expect a radial emission-polarization pattern, while for k-RAT alignment of grains with poor or no internal alignment, we would expect radial, azimuthal, or no polarization, depending on the collisional effects in the flow. This study is aimed at probing for and differentiating between these mechanisms for the carbonaceous dust in the envelope of IRC+10° 216.

1.3. Dust Characteristics

Based both on depletion studies and infrared spectroscopy of circumstellar objects (Whittet 2003) interstellar dust is known to consist of two broad categories: silicate dust, which is expected to possess paramagnetic characteristics (Jones & Spitzer 1967; Draine & Weingartner 1996; Lazarian & Hoang 2019); and carbonaceous dust, which is expected to be diamagnetic (Heremans et al. 1994), including pristine silicon carbide (Wang et al. 2015). Both kinds may contain ferromagnetic inclusions, more likely for the largest grains. Most of the interstellar carbon is thought to originate in AGB stars, but if dust is efficiently reprocessed in the interstellar medium (ISM) composite grains are also possible (Hensley & Draine 2021). As shown by Hu et al. (2019) the dust destruction time for carbon and silicate dust in the ISM is likely different. Hence depending on both destruction and possible reprocessing (in the diffuse ISM) silicate, carbonaceous, and composite grains are mixed. Because of the bigger magnetic susceptibility of silicates, any possible alignment of ISM carbon dust is thus observationally difficult to probe in the ISM.

Support for the importance of the dust bulk magnetic properties on grain alignment is provided by the fact that the silicate spectroscopic feature at 9.7 μm is strongly polarized (Smith et al. 2000). In contrast, the aliphatic CH feature at 3.4 μm, expected to originate from the surface of carbon grains exposed to UV light and atomic hydrogen (Chiar et al. 2013), does not show polarization (Chiar et al. 2006). Recent theoretical work predicts that the CH feature may be polarized, but just below current observational limits (Draine & Hensley 2021), although observational support for this prediction is, as yet, unavailable. In addition to the lack of observed CH line polarization, simultaneous modeling of the UV to near-infrared (NIR) and mid-infrared (MIR) to millimeter-wave polarization (Draine & Fraisse 2009) indicates the need for a cooler, well-aligned dust component and a warmer unaligned component. Since the emission cross sections for the dust are only weakly dependent on mineralogy, while the UV absorption cross section of carbon grains is significantly larger than for silicates (Whittet 2003), we expect carbon grains to be hotter than silicate grains for a given environment, consistent with the observed effects. We note that recent multiband far-infrared (FIR) polarimetry (Gandilo et al. 2016) has not reproduced the strong rise toward longer wavelengths seen in earlier data (Vaillancourt et al. 2008) on which these conclusions are based. Further observations are needed to clarify this discrepancy.

To clarify the effects of mineralogy on grain alignment, a clear observational separation of silicate and carbon dust is needed. In contrast to the ISM, where the different dust components are well mixed, this mineralogical separation is found in the dusty envelopes of AGB stars and related objects, such as some novae (e.g., Gehrz et al. 2018).

Because of the dredge-up of newly processed CNO nuclei associated with the thermal pulsing of the AGB phase (Lattanzio & Wood 2004), such a star and its envelope is expected to transition from its original oxygen-rich phase to one dominated by carbon. This absolute elemental abundance transition is accompanied by a transition in the dust, whereby the initial silicate (and metal oxide) dominated dust material during the early AGB phase (Whittet 2003; Olofsson 2004; Woodward et al. 2021) transitions into a carbon dust (likely SiC and amorphous carbon dust; Ivezić & Elitzur 1996a) dominated circumstellar envelope. Recent observations (Guzman-Ramirez et al. 2015) provide observational evidence that the O-to-C rich history of the shell can, in some sources, be traced through high-resolution observations.

Because of their diamagnetic mineralogy, carbonaceous grains should neither show efficient internal alignment nor be sensitive to the magnetic field, and thus any alignment would be expected to be due to some nonmagnetic aligning mechanism. A minor fraction of metallic iron grains are possible also in C-rich AGBs based on condensation theory (Gail & Sedlmayr 2013) and supported by depletion studies (Mauron & Huggins 2010). If such grains are incorporated into predominantly carbonaceous solids (more likely for the largest grains; see Mathis 1986), some response to an ambient magnetic field may be possible.

We here discuss the case of the carbon-rich AGB star IRC +10° 216. We have also acquired Stratospheric Observatory for Infrared Astronomy (SOFIA)/High-resolution Airborne Wideband Camera-plus (HAWC+) observations of the oxygen-rich CSE around IK Tau. As shown by Fox-Middleton et al. (2021), and as will be discussed more fully in a future paper, the polarization geometry in that CSE is neither radial nor azimuthal but can be fitted with a projected dipole

Table 1
Polarimetric Observations Log

Band	λ_c (μm)	$\Delta\lambda$ (μm)	Pixel Scale ($''$)	Beam Size ($''$)	Date (YYYY/MM/DD)	Flight	Chop Angle ($^\circ$)	Chop Throw ($''$)	# Sets	On-source Time (s)
A	53	8.7	2.55	4.85	2016/12/14	F358	0	180	16	1280
C	89	17	4.02	7.80	2016/12/08	F356	0	180	9	700
D	154	34	6.90	13.60	2017/11/16	F453	0	150	2	760
							90	150	2	800
E	214	44	9.37	18.20	2016/12/14	F358	0	180	5	380
					2016/12/15	F359	0	180	13	1040

structure. While we will not describe or discuss this source in detail here, we note that these results indicate that the polarization geometry reported here is not solely due to the source structure but is intimately related to the dust characteristics in IRC+10° 216.

1.4. IRC+10° 216

Here, we present FIR photometry and polarimetry of the carbon-rich star IRC+10° 216 with the HAWC+ instrument on the SOFIA, analyzed in the context of archival data from Herschel/Photodetector Array Camera and Spectrometer (PACS) and recent optical polarimetry results toward stars background to the CSE. These data are used to analyze and interpret the alignment of carbon dust in a high-radiation environment, specifically in the context of RAT theory.

IRC+10° 216 is a well-known infrared object discovered at 5 μm in 1969 (Becklin et al. 1969) and identified as a dust-enshrouded carbon star by Miller (1970). Because of the brightness and proximity ($d = 123 \pm 14$ pc; Groenewegen et al. 2012) it has been extensively studied both in continuum and line radiation (e.g., Cernicharo et al. 2010; Decin et al. 2011, and references therein). The central AGB star CW Leo (for clarity, we will henceforth refer to the star by that name and the CSE object as IRC+10° 216) is surrounded by an extensive dust and gas shell terminated in a termination shock, where the CSE runs into the ISM, seen in both the UV (Sahai & Chronopoulos 2010) and the FIR (Ladjal et al. 2010). The central star is estimated to have had an initial mass of 3–5 $M_\odot$ (Guelin et al. 1995), which has decreased to a current value of about 0.7–1.0 $M_\odot$ (Ladjal et al. 2010). Because of its high C/O ratio (C/O = 1.4; Milam et al. 2009, and references therein), the dust in the CSE is fully carbonaceous (95% amorphous carbon and 5% SiC by mass; Ivezić & Elitzur 1996a). While atomic iron has been detected in the CSE of IRC+10° 216 (Mauron & Huggins 2010) and shows significant depletion, no direct observational evidence is yet available for iron grains or iron inclusions in the carbon grains.

While the star is surrounded by a visually opaque envelope, NIR speckle and aperture-masking interferometry (e.g., Weigelt et al. 1998; Tuthill et al. 2000), as well adaptive-optics-supported polarimetry (e.g., Murakawa et al. 2005), have provided insights about the very-small-scale structure around the star. These studies point to a circumstellar torus, seen close to edge-on and oriented at ~120°, with a bipolar cavity oriented at ~20° (Murakawa et al. 2005). Together, these imply a stellar rotation axis nearly parallel to the plane of the sky.

Evidence for magnetic fields in IRC+10° 216 has been provided through both observations of the Goldreich–Kylafis effect in several molecules (Girart et al. 2012) with the Sub-mm

Array (SMA) and through Zeeman observation in the $J = 1$–0 line of CN (Duthu et al. 2017) with the IRAM 30 m, single dish telescope. On the small scales probed by the SMA, Girart et al. (2012) say that they: "[…] infer that the magnetic field configuration has a global radial pattern […] but [that] it possibly has a rather complex magnetic field morphology." The $J = 1$–0 line of CN Zeeman observation Duthu et al. (2017), however, shows significant spatial variations, including field direction reversals, in the derived (line-of-sight) field strength around the central star, indicating deviation from spherical symmetry.

2. Observations and Data Reduction

Observations of IRC+10° 216 were acquired with the HAWC+ (Vaillancourt et al. 2007; Dowell et al. 2010; Harper et al. 2018) on the 2.7 m SOFIA under proposal IDs 04_0119 and 05_0048 (PI: Andersson). Polarimetric observations with HAWC+ simultaneously measure two orthogonal components of linear polarization in two arrays of 32×40 pixels each. We used four bands, with their characteristic central wavelength, bandwidth, pixel scale, and beam size shown in Table 1. For all bands, we performed observations in a four-positions dither square pattern with a distance of three detector pixels in the sky coordinates system (ERF), where positive increase of angles are in the east of north direction. In each dither position, four half-wave plate (HWP) position angles (PAs) were taken in the standard sequence 5°, 50°, 27°.5, and 72°.5. A dither sequence of four HWP PAs is called a "set" hereafter. We used a chop frequency of 10.2 Hz, and nod times of 30 s, 40 s, and 50 s, with the rest of the observational configurations listed in Table 1. The final on-source times used for data analysis are 1280 s, 700 s, 3785 s, and 1420 s for bands A, C, D, and E, respectively. The chop-nod technique and internal calibrators have an overhead of 2.45 times. Thus, the final execution times of the observations are 3136 s, 1715 s, 9273 s, and 3479 s for bands A, C, D, and E, respectively.

Data were reduced using the HAWC_DRP_PIPELINE V1.1.1. The pipeline procedure described by Harper et al. (2018) was used to background subtract and flux calibrate the data and compute Stokes parameters and their uncertainties. Final degree and PA of polarization accounts for correction of instrumental polarization, bias, and polarization efficiency. Typical standard deviations of the polarization after subtraction of ~0.3% are estimated for all bands. The data were reduced to have a pixel scale equal to one-quarter of the beam size (4×4 pixels per beam), and images were then smoothed using a Gaussian profile with a FWHM equal to the beam size of the observations. The pixels are, therefore, correlated within an angular resolution equal to the beam size. Final reduced images have a pixel scale of 1″.21, 1″.95, 3″.40, and 4″.55 for bands A,
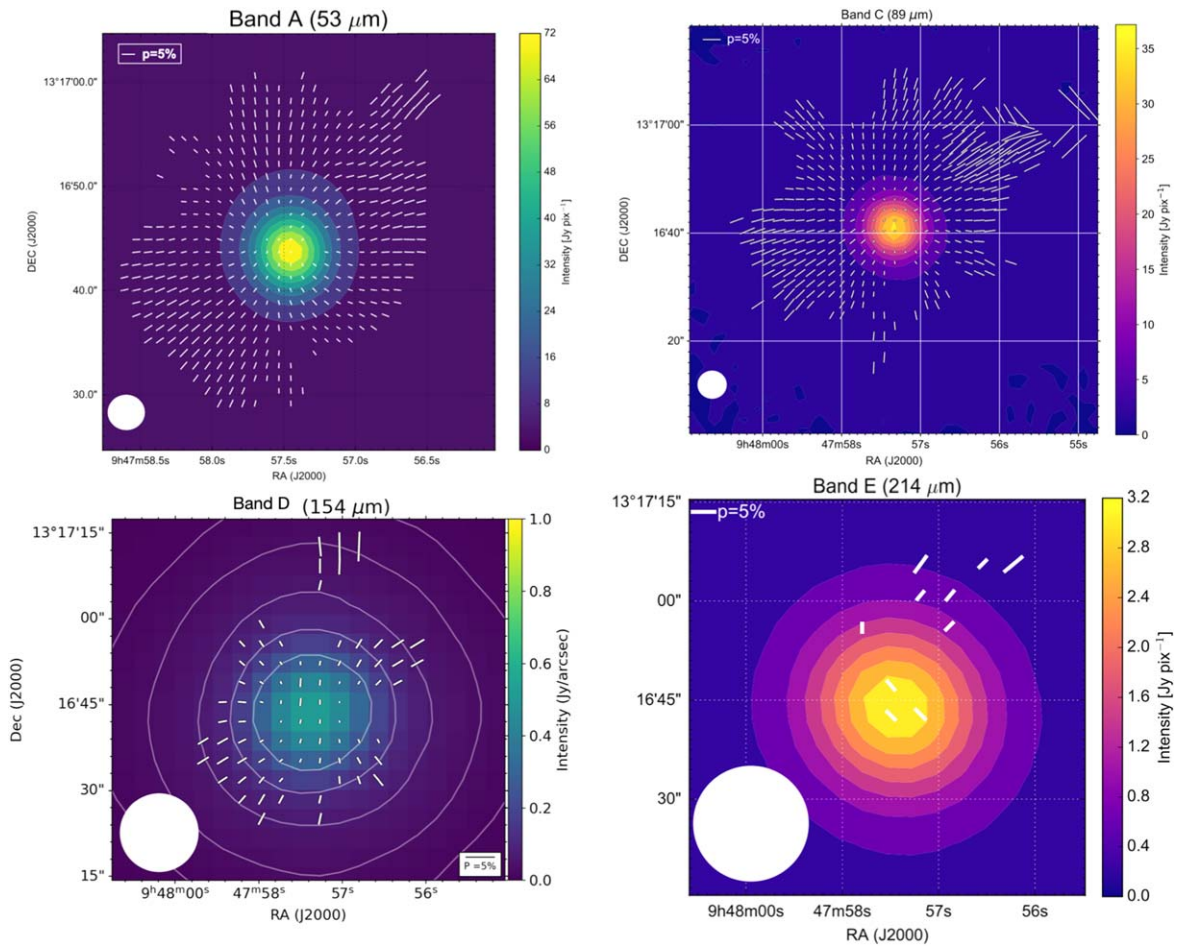
Figure 1. HAWC+ intensity map (color map) with polarization vectors overplotted (white vectors) for all bands. Only polarization measurements where S/N $\geqslant$ 5 are shown. The field of view shown is $60'' \times 60''$. The beam sizes shown with white circles for bands A, C, D, and E are $4\rlap{.}''9$, $7\rlap{.}''8$, $13\rlap{.}''6$, and $18\rlap{.}''2$, respectively.

C, D, and E, respectively. Further analysis and high-level displays were performed with custom PYTHON routines. Figure 1 shows the polarization maps (E-vectors) of IRC+10° 216 for each band with polarization measurements of $P/\sigma_P \geqslant 5$ shown. To, perhaps, more clearly emphasize the radial polarization geometry, we show in Figure 2 the Band A map with only every second vector drawn and enlarge the central part of the Band C map.

We acquired additional total-intensity observations using the on-the-fly-map (OTFMAP) observing mode for each band. We performed OTFMAPs using a Lissajous pattern, with the scan amplitude, phase, and duration shown in Table 2. An example of this observing mode is shown in Lopez-Rodriguez et al. (2018, Figure 1). The data were reduced using the Comprehensive Reduction Utility for SHARP II v.2.42-1 (CRUSH; Kovács 2006, 2008) and the HAWC_DRP_V1.1.1 pipeline. Each scan was reduced by CRUSH, which estimates and removes the correlated atmospheric and instrumental signals, solves for the relative detector gains, and determines the noise weighting of the time streams in an iterative pipeline scheme. Final reduced images have a total on-source time of 160 s, 200 s, 600 s, and 300 s, for bands A, C, D, and E, respectively, with pixel scales of $1\rlap{.}''00$, $1\rlap{.}''55$, $3\rlap{.}''40$, and $3\rlap{.}''70$. Due to tracking and readouts, the OTFMAPs have an overhead of 1.1 times. Thus, the final execution times of the observations are 176 s, 220 s, 660 s, and 330 s for bands A, C, D, and E, respectively.
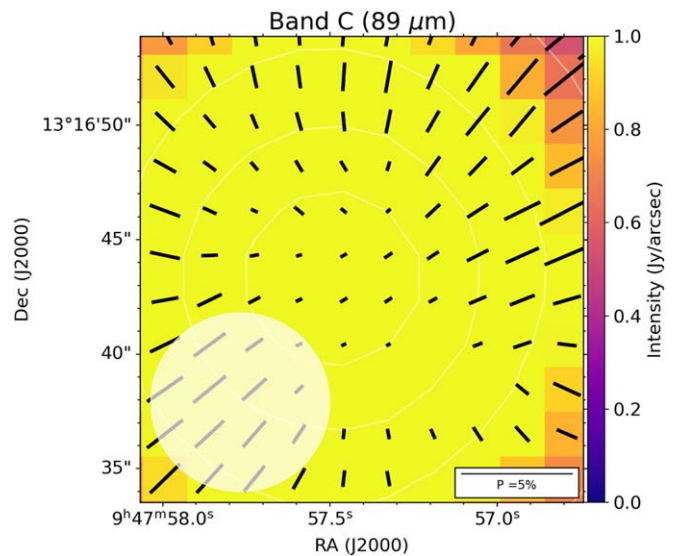
Figure 2. Central zoomed-in view of polarization vectors in band C. The band C beam is shown in the lower-left corner.

Due to the brightness of IRC+10° 216, the observations in Band D are affected by cross talk along the chop direction. Specifically, we found a large angular dispersion that displaced the PA of polarization away from the azimuthal pattern seen in
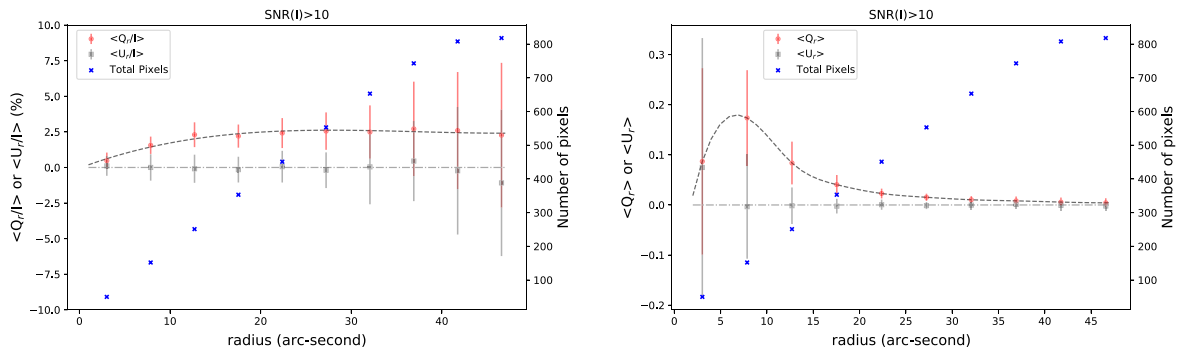
Figure 3. Radial polarization SOFIA HAWC+ Band A. Left: averaged Q_r/I (green) and U_r/I (red). Right: Q_r and U_r, indicating radial polarization by $Q_r/I(Q_r) > 0$ and $U_r/I(U_r \simeq 0)$. The number of data points for each annulus are plotted as blue symbols. The gray curves are spline fits to the Q_r/I (Q_r) but are intended solely as a guide to the eye. The beam size of the HAWC+ Band A is $4''.85$.

Table 2
Total-intensity Observations Log

Band	Date (YYYY/MM/DD)	Flight	Scan Time (s)	Scan Angle (°)	Scan Amplitude (E L× XEL, ")	# Scans
A	2016/12/14	F358	80	0.0	40 × 40	2
C	2016/12/14	F358	100	0.0	60 × 60	2
D	2017/11/16	F453	60	−30, 30	70 × 70	4
			120	−30, 30	70 × 70	3
E	2016/12/14	F358	100	0.0	150 × 150	2

the other regions of the source at this and other bands. Therefore, we excluded Band D from our modeling.

For information concerning the observation of IRC+10° 216 and subsequent data reduction of the Herschel/PACS images, see Ladjal et al. (2010).

3. Analysis

3.1. Radial Polarization

Based on initial inspection of the SOFIA/HAWC+ data, the emission and polarization is close to centrosymmetric (Figure 1), particularly in HAWC+ Band A. To quantitatively characterize this impression we transformed the observer's system polarization to radial Stokes parameters, Q_r and U_r, as described in Equation (1), where the Poincaré sphere's reference frame is rotated by the polar angle at each point with respect to the star location:

$$Q_r = +Q \cos 2\phi + U \sin 2\phi$$
$$U_r = -Q \sin 2\phi + U \cos 2\phi, \tag{1}$$

where $\phi = \arctan \frac{\alpha - \alpha_0}{\delta - \delta_0}$ is the polar angle of a given position (α, δ) (equatorial coordinate) and (α_0, δ_0) is the location of the star. We here focus the quantitative analysis to the Band A data. This is partially due to the smaller beam size for the 53 μm data, providing higher spatial resolution, but also because the longer bands are, relatively, less sensitive, yielding fewer polarization measurements.

Positive Q_r indicates radial polarization, while negative Q_r points to evidence for tangential polarization. U_r represents polarization with an angle of $\pm 45°$ from the radial direction. Therefore, zero U_r implies purely radial ($Q_r > 0$) or tangential ($Q_r < 0$) polarization. This methodology has previously been utilized to study the radial polarization in Uranus and Neptune

(Schmid et al. 2006) and in protoplanetary sources (Canovas et al. 2015).

We averaged Q_r and U_r for several annuli around the star, as shown in Figure 3. The left panel shows the radial Stokes parameters normalized by the Stokes I at each location and the error bars show the standard deviation of Q_r/I and U_r/I (over the azimuthal angles) in each annulus. The positive $\langle Q_r/I \rangle$ and zero $\langle U_r/I \rangle$ indicate a fully radial polarization pattern. The radial profile of $\langle Q_r/I \rangle$ increases in value from the star's location to a radius of about $50''$ and then slowly drops to zero. This is likely a combination of the projection effect inherent in radial polarization from a spherical source (Section 3.4) at small radii, and the decrease in inherent polarization at large radii.

3.2. Radial Averaging of the Data

Because our primary goal is to probe the grain alignment (and dust temperature) as a function of radius, and as the polarization shows a fully radial geometry, we will generate and analyze azimuthally averaged radial profiles in intensity and polarization, to enhance the signal-to-noise (S/N) on our analysis. Although the IRC+10° 216 shell is known to contain multiple dust shells, including azimuthal variations (Mauron & Huggins 1999, 2000), for our purposes azimuthally averaged data are expected to serve as a fair approximation and capture the physics of the grain alignment. Figure 4 shows that the approximation is very good for the intensity profile, while the polarization variations are somewhat larger. A detailed study of the full 3D polarized radiative transfer modeling of the CSE is outside the scope of this current study.

For comparisons with our model calculations, azimuthally averaged intensities (HAWC+ and PACS data) and polarization (HAWC+ data) are then radially averaged into bins matching the beam sizes of the HAWC+ data and the pixel sizes of the Herschel/PACS archival images (Table 3).

6
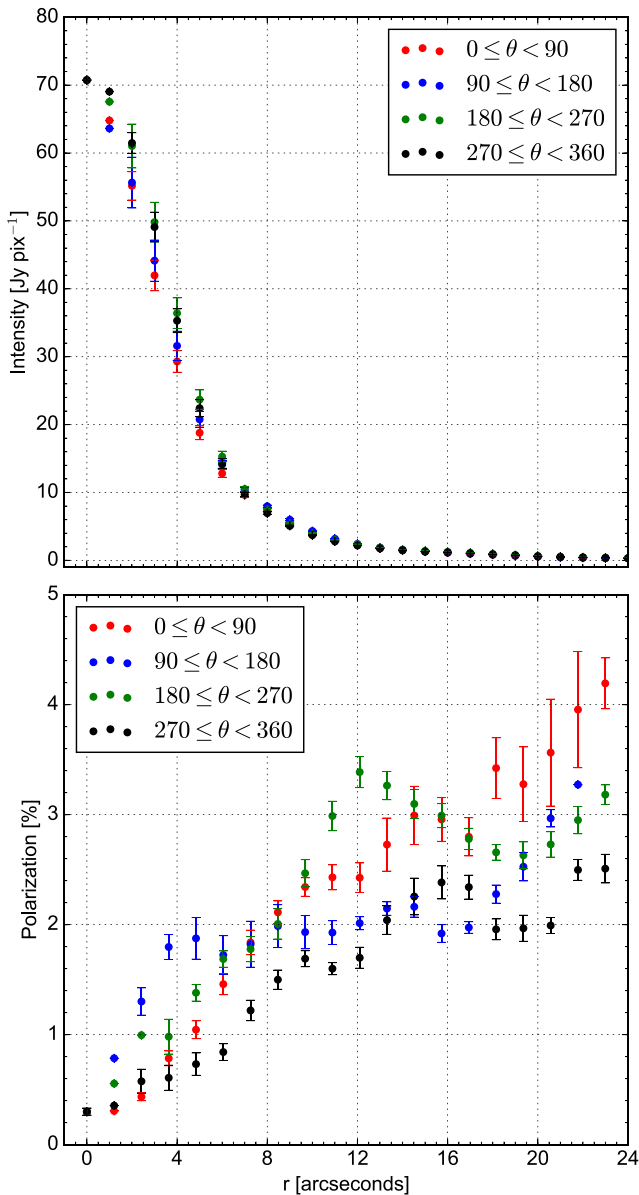
Figure 4. Radially averaged intensity (upper panel) and polarization (lower panel) profiles in quadrants for HAWC+ Band A measurements. For all averages, only data where $S/N \geqslant 5$ were considered. An azimuthal angle of $0°$ is described as the eastern axis and increase north of east. The beam size of the HAWC+ Band A is $4''.85$. The data are oversampled in this figure to indicate possible small-scale variability.

3.3. Temperature Modeling—DUSTY

In order to fit the observed azimuthally averaged intensity profiles from our images, we used the DUSTY radiative transfer code (Ivezic & Elitzur 1997). DUSTY solves the one-dimensional radiative transfer equations assuming that the dust density distribution surrounding a central source is spherically symmetric. DUSTY creates a model of a CSE based on user-input optical properties, mineralogy, and size distribution of the dust grains, the physical properties of the central source, dust sublimation radius or temperature, and dust density distribution in the CSE. Based on these input parameters, the code outputs an intensity profile for a given set of wavelengths and the dust temperature, along with additional information concerning the spectral energy distribution (SED) of the source. We will

Table 3
FWHMs (in Arcseconds) of Gaussian Kernels Used in Model Convolution and Pixel Sizes (in Arcseconds) of each Image

Image	Kernel FWMH		Pixel Size	
	Beam	Smoothing	Intens.	Pol.
HAWC+ Band A	4.7	2.57	1.0	1.21
HAWC+ Band C	7.8	4.02	1.55	1.95
HAWC+ Band D	14	…	3.4	3.4
HAWC+ Band E	19	9.43	3.7	4.55
PACS 70[a]	…	…	1.6	…
PACS 160[a]	…	…	3.2	…

Note.
[a] The point-spread function (PSF) used to convolve the PACS images cannot be estimated by a Gaussian kernel. As a result, we have used the PSF for each band from Bocchio et al. (2016).

exclude the HAWC+ Band D image for our modeling since the different scanning pattern used for this observation caused an instrumental artifact in this image. Because DUSTY provides outputs in dimensionless quantities, we will primarily be examining the normalized intensity profile for each of our images.

3.3.1. Model Assumptions

For the grain mineralogy, we adopted a composition of 95% amorphous carbon and 5% SiC by mass (Ivezić & Elitzur 1996a). The absorption and scattering coefficients are calculated using Mie theory based on this grain composition. The optical properties for amorphous carbon were taken from Hanner (1988) and those for SiC from Pegourie (1988). We used a modified Mathis–Rumpl–Nordsieck (MRN; Mathis et al. 1977) grain size distribution from Kim & Martin (1994) of $n(a) \propto a^{-q} e^{-\frac{a}{a_0}}$, with $q = 3.5$, $a_{min} = 0.005$ μm, and $a_0 = 0.2$ μm (Jura 1994; Ivezić & Elitzur 1996a).

In an effort to reduce the number of free parameters in our model we fixed the stellar temperature and luminosity in the modeling, based on values from the literature. The stellar properties are fairly well constrained as multiple studies find similar results. With one exception, the effective temperature of CW Leo has been estimated at $T \sim 2200$ K (2230 K (Cohen 1979), 1800 K (Phillips et al. 1982), 2330 ± 350 K (Ridgway & Keady 1988), 2200 ± 150 K (Ivezić & Elitzur 1996a), 1915–2105 K (Bergeat et al. 2001), and 2330 K (Agúndez et al. 2012)). Menten et al. (2012) used the Very Large Array, with 40 mas resolution, to derive the luminosity of CW Leo from the brightness temperature of the radio photosphere. These findings were also consistent with radiative transfer model findings based on observations from the IRAM 30 m telescope and with Herschel/HIFI by De Beck et al. (2012). With our assumed distance of 123 pc, the consistent luminosity found by Menten et al. (2012) and De Beck et al. (2012) is equivalent to $\sim$8640 $L_\odot$. We will then assume these stellar parameters for the subsequent thermal modeling.

We will also need to define the dust density distribution in the CSE. Generally, we have assumed IRC+10° 216 to be surrounded by azimuthally symmetric dust shells where the dust density for each shell decreases with r^{-2} from the central star. However, several dust shells have been observed in the optical out to $50''$ from CW Leo, which have varying thicknesses from $\sim 0''.5$–$3''$ (Mauron & Huggins 1999, 2000).

Table 4
Fitted Parameters to Our Measured Intensity Profiles Using our DUSTY Model

Parameter	Units	Fitted Values	Bounds
τ_{λ_0}	⋯	0.018	[0, 0.1]
$C_{s,1}$	⋯	19.07	[0, 20]
$C_{is,2}$	⋯	0.61	[0, 10]
$C_{s,2}$	⋯	9.96	[0, 20]
$C_{is,3}$	⋯	4.05	[0, 10]
$C_{s,3}$	⋯	8.27	[0, 20]
$C_{is,4}$	⋯	1.92	[0, 10]
$C_{s,4}$	⋯	8.33	[0, 20]
C_{os}	⋯	1.78×10^{-4}	[0, 0.1]
r_{sub}	″	0.348	[0.15, 0.4]
r_1	″	2.63	⋯
t_1	″	1.56	[0.5, 3]
r_2	″	10.26	⋯
t_2	″	1.57	[0.5, 3]
r_3	″	19.25	⋯
t_3	″	0.92	[0.5, 3]
r_4	″	26.01	⋯
t_4	″	1.633	[0.5, 3]
L_{st}[a]	$L_\odot$	8640	⋯
T_{st}[a]	K	2200	⋯

Note. In the above table the parameters listed correspond to the following descriptions: τ_{λ_0} is the total optical depth at 100 μm; C is the density contrast, where $C_{s,i}$ corresponds to the contrast in the ith shell and $C_{is,i}$ corresponds to the contrast within the ith shell; C_{os} corresponds to the density contrast outside of the shells; r_{sub} is the dust sublimation radius; r_i and t_i correspond to the radius and thickness of a shell, respectively, where r_i (with the exception of r_1) was parameterized by $r_i = r_{i-1} + t_{i-1} + \Delta_i$ in our model (i.e., Δ_i was the actual parameter fitted); L_{st} is the luminosity of IRC+10° 216; and T_{st} is the effective temperature of IRC+10° 216. No bounds are listed for the radii as they are parameterized by $r_i = r_{i-1} + t_{i-1} + \Delta_i$. For all Δ_i, the bounds imposed were [0, 10].
[a] Fixed parameters.

These dust shells are thought to be the result of multiple mass-loss episodes, with different mass-loss rates (Mauron & Huggins 2000). These varying mass-loss rates manifest as relative density increases, or decreases, between various shells (i.e., $\rho(r) \propto Cr^{-2}$ for various regions, where C is the "density contrast" and is defined as 1 for the innermost shell). Optical observations show four prominent dust shells out to a distance of 40″ (Mauron & Huggins 2000). We therefore assume four dust shells when creating our density distribution.

Finally, we need to define the total dust mass, or equivalently a total opacity, as the density profile provided is in dimensionless units. Ivezić & Elitzur (1996a) modeled the total optical depth at 100 μm and found $\tau \sim 0.01$, which we use as our approximation of shell opacity.

3.3.2. Model Optimization Procedure

To derive the physical characteristics of the CSE, we have assumed values for the dust composition, size distribution, and the physical properties of the source. The rest of the parameters for the dust distribution (summarized in the notes of Table 4) were fitted through optimization. For a set of parameters, we created images for each wavelength using the DUSTY model, with the same pixel sizes as our observed images, and convolved each model image with the point-spread function for each observation (see Table 3). Finally, the radially averaged intensity profiles (out to a distance of ~40″) were compared with the observed profiles.

As for many multiparameter optimization problems, we expect there to be multiple local minima over a quite complex optimization surface. As a result, using classical optimization methods, like nonlinear least squares or some simplex regression method, on their own may not be adequate in producing an optimal solution, and the results might be highly dependent on the selected initial conditions. To overcome these limitations, we employed a stochastic optimization method, which is better equipped to find a global minimum. We therefore employed a method called "differential evolution" optimization, described more fully in the Appendix A. In the appendix we also describe the use of synthetic data sets to evaluate the effectiveness of our optimization procedure.

Differential evolution belongs to a category of evolutionary algorithms in which a population of candidate solutions are successively adapted until a desired threshold or some number of iterations are reached. Differential evolution was originally introduced by Storn & Price (1997) and is ideal for optimization problems that are nondifferentiable, noncontinuous, or have many local minima. Besides the adaptation strategy, differential evolution is capable of searching the parameter space in a continuous manner.

Differential evolution operates by first evaluating a random population of trial solutions within user-defined parameter bounds. This is followed by the steps of "mutation" and "recombination," which generate new solutions to be compared to observational constraints. The best solutions are then selected and the process of mutation, recombination, and selection is repeated until the maximum number of generations are reached, or when the standard deviation in fitness values for a given generation falls below a user-defined threshold. Following the completion of such a routine, the results are often used as the starting point for a least-squares optimization to "polish" the final result. It should, however, be noted that there is no proof of convergence for differential evolution minimization.

First we will consider what can practically be determined from the observations. Because there is no proof of convergence for differential evolution optimization, we performed a fit to three synthetic data sets in order to evaluate the effectiveness of our optimization procedure. The creation of and results from fitting these synthetic data sets are discussed in Appendix B.

As shown by Ivezić & Elitzur (1996b), the profiles for infrared images of late-type stars, when the grain composition and size distribution are fixed, are primarily determined by the overall optical depth and the dust sublimation radius. For small optical depths, such as those expected for the wavelength regimes probed in our study, the relative intensity profile is proportional to the relative optical depth along each sight line. This relative intensity can then be scaled to the true intensity based on the overall optical depth. The temperature profile depends on the intensity and the optical depth, but for optically thin emission the extracted temperature depends sensitively on the derived optical depth.

In order to correctly scale the relative temperature profile, the dust sublimation temperature must be determined by resolving for the sublimation radius (Ivezić & Elitzur 1996b):

$$T_{\rm sub} = T_{\rm st} \sqrt{\frac{R_{\rm st}}{r_{\rm sub}\alpha}}. \qquad (2)$$
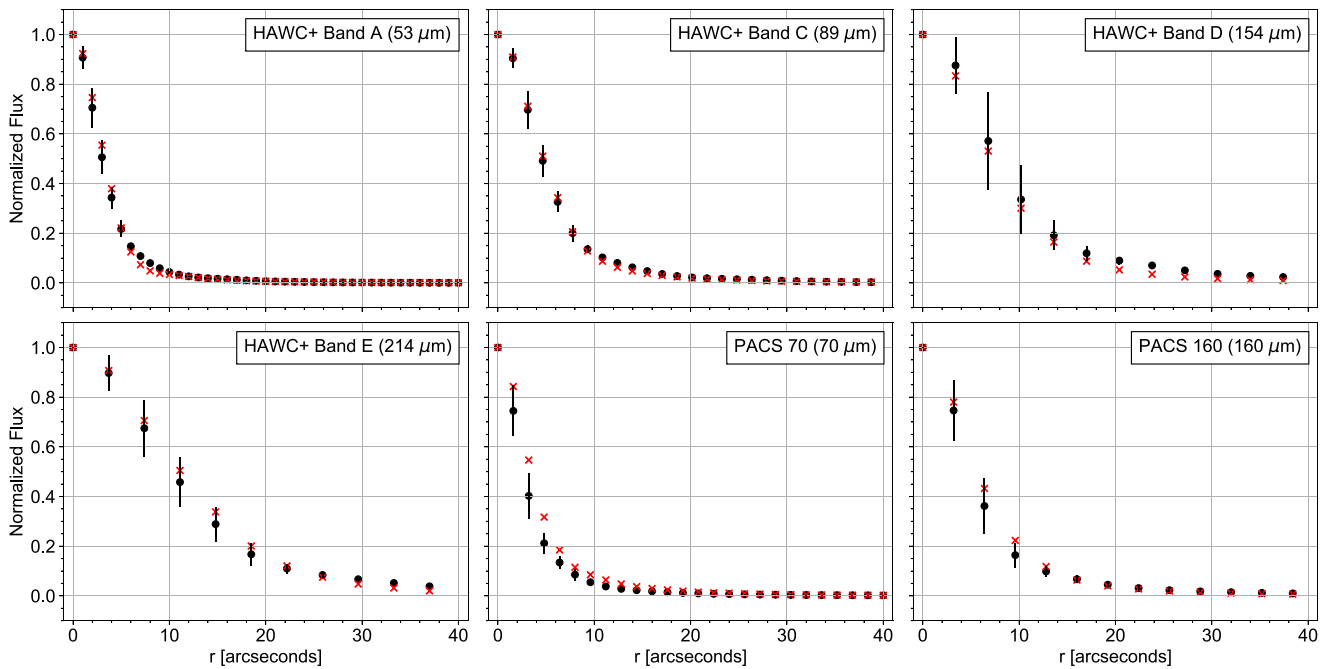
Figure 5. Radial profiles of the measured (black data points) and modeled (red ×'s) normalized intensity profiles for each image. The beam sizes of HAWC+ bands A, C, D, and E are shown in Figure 1. The beam sizes of the PACS 70 μm and 160 μm are 5''6 and 10''7, respectively.

In this equation the dimensionless quantity α is dependent primarily on the grain chemistry and only weakly on the overall optical depth.

As discussed by Ivezic & Elitzur (1997), for a CSE observed in the optically thin regime (Ivezić & Elitzur 1996b), there are two options to determine the sublimation radius. The first is to obtain high-resolution observations where the dust condensation zone can be resolved. The second is to determine this value from the SED of the source. Because of the limited spatial resolution of our data and the fact that our wavelengths are in the Rayleigh−Jeans limit of the emission, our data are not directly able to reliably determine the sublimation temperature. This limits our ability to determine the absolute temperature profile.

However, for the current study the overall, relative shape of the temperature profile and how it compares to the polarization measurements is more important. From the synthetic data fits we find the temperature profile is simply scaled compared to the true profile by a single scaling factor outside of the beam. Therefore, the relative shape of the profile is likely correct, which is in accordance with the conclusions from Ivezić & Elitzur (1996b).

3.4. Deprojected Polarization

Our goal is to compare the temperature profile of the material surrounding IRC+10° 216 to the polarization-efficiency profile. Since dichroic polarization probes the direction perpendicular to the alignment axis, we therefore need to deproject the polarization profile described in Section 3.2. Because we observe the polarization—and, by implication, the grain alignment—to be radial, we are able to "deproject" the polarization (i.e., separate inherent and observed polarization) by $p = p_0 \sin(\alpha)$, where α is the angle between the radial shell from the star and the line of sight (i.e., $\sin(\alpha) = \frac{r}{R}$, where r is the distance on the sky and R is the radius of the shell). We can

then scale the deprojected polarization to the temperature linearly to compare them:

$$T \propto p_{\text{scaled}} = Cp\frac{R}{r} + B. \tag{3}$$

Since there are multiple (optically thin) shells surrounding IRC+10° 216, the choice of R is somewhat arbitrary. We have set it to the outer distance of the largest shell. The scaling parameters C and B are then left as free fitting parameters. To ensure reliable results, we restrict the analysis to measurements with $S/N \geqslant 5$. We therefore focus on HAWC+ Band A and Band C. A more accurate deprojection requires a full polarized radiative transfer model, which we will present in a future paper.

4. Results

4.1. Observational Data Fits

The best fit to our azimuthally averaged intensity profiles and the optimized dust density parameters are shown in Figure 5 and Table 4. While we did not use the Band D data for our fit, we have included the predicted profile from the DUSTY model compared to the observed data. With these parameters, good overall fits to the radially averaged intensity profiles are achieved. We find an overall reduced chi-squared of 4.96. The derived radii are in reasonable agreement with the location of most of the shells observed by Mauron & Huggins (2000), who observed shells at $\sim10''$, $\sim18''$, $\sim25''$, and $\sim33''$.

The resulting temperature profile is shown in Figure 6. While our modeled dust temperature aligns with the dust temperature derived from a modified blackbody by Decin et al. (2011; Figure 6, data point), the analytical profile approximated from the SED modeling of Decin et al. (2011; Figure 6, dashed line) is lower by ~35 K and decreases faster at larger radii.
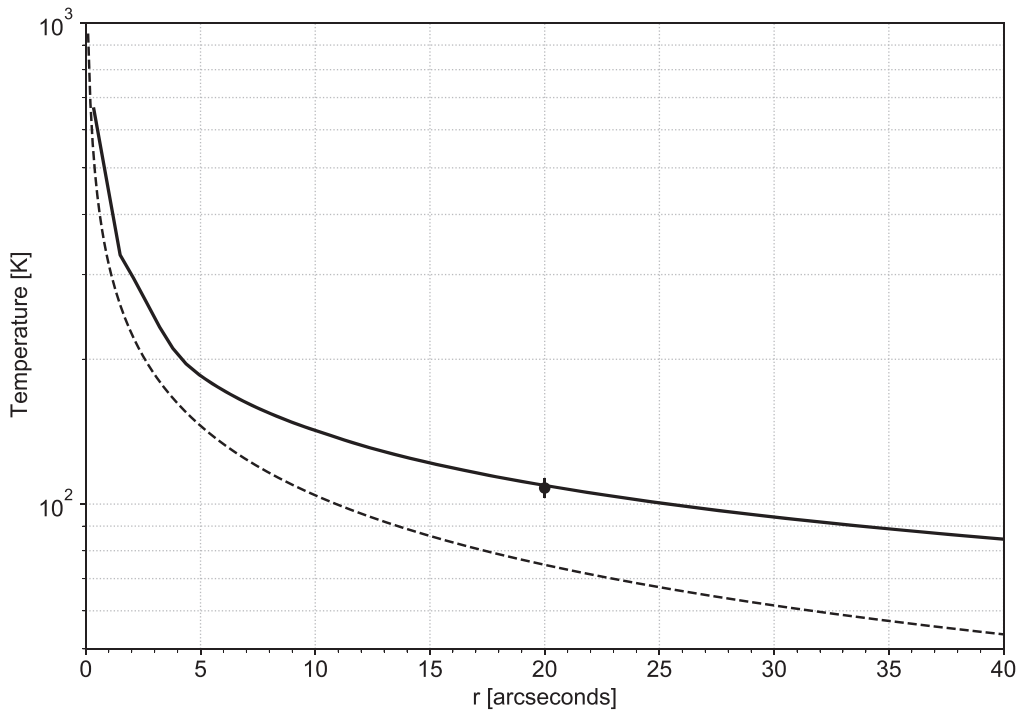
Figure 6. The modeled temperature profile fitted to our data as a function of radius from the center of the source. The solid black line corresponds to our fitted temperature profile using DUSTY, the dashed black line corresponds to the modeled temperature profile from Decin et al. (2011), and the data point corresponds to the derived dust temperature at $20''$ from Decin et al. (2011).

4.2. Comparing Deprojected Polarization

The scaled, deprojected, polarization based on Equation (3) is shown in Figure 7 for HAWC+ bands A (closed circles) and C (open circles). The data points shown are for distances greater than their respective beams and less than the outermost shell found in our model (i.e., $24''.5$). We find a tight linear correlation between temperature and polarization, yielding reduced chi-squared values of 3.9 and 3.5 for bands A and C, respectively. As shown by, e.g., Medan & Andersson (2019), Soam et al. (2021), and Santos et al. (2019), the grain alignment—i.e., radiative spin-up rate—in the ISM is proportional to the intensity of the illuminating radiation. Further, the grain temperature is directly dependent on the illumination strength. Because the CSE has a steep (negative) density gradient and is optically thin for most wavelengths (which would apply to reprocessed short-wavelength radiation), we expect the radiation field to drop off symmetrically from the star, and that it should be highly anisotropic, as required for RAT alignment, and we interpret the radial correlation between dust temperature and polarization to indicate that, also in the CSE, both temperature and alignment are directly dependent on the radiation field strength.

4.3. Wind Modeling

Because Gold, MET, and secondary k-RAT alignment (see Section 1) all depend on systematic gas–grain flows, we have explored the nature of the AGB wind, and specifically the drift velocity, in the CSE of IRC+10° 216.

Based on a comparison between the radiation pressure on dust grains (Kwan & Hill 1977) and stationary wind models (Ramstedt et al. 2008, see their Table 6), existing studies estimate a drift velocity in the CSE of $v_D \simeq 2$ km s^{-1}. For example, Habing et al. (1994) derived analytical expressions

for the relationship between the stellar luminosity (L_*), mass-loss rate ($\dot{M}$), and gas–dust drift velocity (v_D):

$$v_D \propto \frac{L_*}{\dot{M}c} v_{\text{exp}}. \tag{4}$$

Using a time-dependent approach to the stellar wind, we now show that drift velocities become much higher than with a stationary approach. We employed the numerical codes developed by Sandin (2008) and refined as the T-800 model by Sandin & Mattsson (2020), which suggest a typical drift velocity of $v_D \simeq 10.0$ km s^{-1} rather than $v_D \simeq 2.0$ km s^{-1}. We note that we are not attempting to achieve detailed agreement between the DUSTY modeling and the AGB wind models, as these simulations are very resource intensive and our primary aim is to address the grain-alignment process.

Because CW Leo is likely cooler but more luminous than the parameter phase space explored so far by the T-800 models, we carried out dedicated model runs for IRC+10° 216. Owing to the low resulting expansion velocities, we calculate the stellar wind models out to 20 R_*, where the output parameters in Table 5 are evaluated as averages over a longer time interval. We assume that the radial structures in the gas and dust velocities are unchanged out to larger radii, in agreement with the results in Sandin & Mattsson (2020). Of course, density-dependent entities such as the sound speed, as well as gas and dust temperatures, are expected to fall with radius, beyond the limit of our models. As the stellar photosphere is estimated to have a projected radius of 42 mas (Menten et al. 2012), our beam size of $4.85''$ (Band A) corresponds to ~115 R_*, and hence does not resolve the modeling range. Here, we only report a summary of the model results. Further details will be discussed separately (C. Sandin et al., 2022, in preparation).

We found that for the nominal luminosity and temperature of $L = 8640$ $L_\odot$ and $T_{\text{eff}} = 2200$ K (see Section 3.3.1), dust-driven
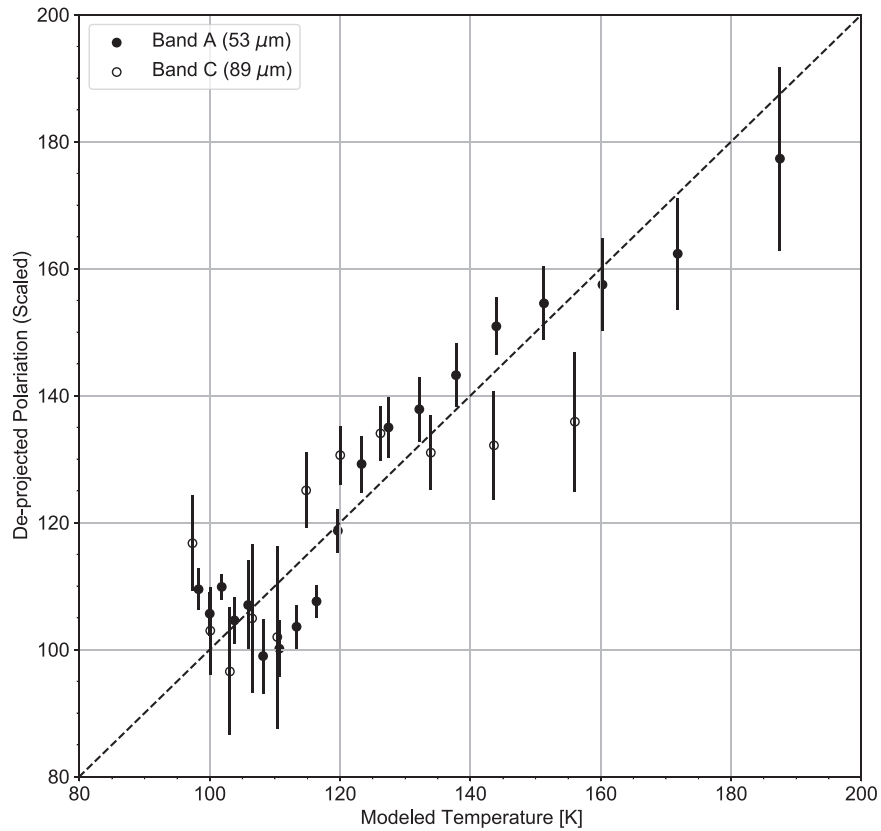
Figure 7. The scaled, deprojected polarization for HAWC+ Band A (closed circles) and Band C (open circles) plotted vs. the fitted temperature from the DUSTY model. The dashed line shown is the line for a 1-to-1 relationship. The scaling parameters for the Band A fit resulted in $C = 22.71 \pm 1.67$ and $B = 14.97 \pm 8.43$. The scaling parameters for the Band A fit resulted in $C = -31.33 \pm 8.01$ and $B = 230.3 \pm 28.61$.

Table 5
Modeled Wind Parameters for IRC+10° 216

L_* [$L_\odot$]	$T_{\rm eff}$ [K]	M_* [$M_\odot$]	$\dot{M}$ [$10^{-5}\,M_\odot\,{\rm yr}^{-1}$]	$v_{\rm exp}$ [km s^{-1}]	$v_{\rm D}$ [km s^{-1}]	$f_{\rm cond}$	$\dot{M}_{\rm d}/\dot{M}$	$r_{\rm d}$ [μm]
9,000	2100	0.6	2.6	5.8	10	0.15	0.0007	1.3
10,000	2100	0.6	3.1	6.6	11.0	0.09	0.0005	0.9
12,000	2100	0.6	4.8	8.2	9.7	0.08	0.0005	0.8
18,000	2200	0.6	7.9	9.6	9.8	0.09	0.0004	0.9
18,000	2300	0.6	5.3	8.9	11.4	0.07	0.0003	—
18,000	2100	1.0	2.2	4.9	15.1	0.13	0.0006	0.9

wind formation did not occur. At $L = 9000\ L_\odot$ and $T_{\rm eff} = 2100$ K, a slow wind is generated using the additional parameters $\log(C - O)+12 = 8.20$ (corresponding to C/O = 1.35) and $M = 0.6\,M_\odot$, and dust opacities calculated using Mie theory. All other physical assumptions and parameters, as well as the numerical approach, are the same as in Sandin & Mattsson (2020); in particular, the models assume spherical dust grains. At this relatively low luminosity, a wind is generated with a mass-loss rate of $\dot{M} = 2.6 \times 10^{-5}\,M_\odot\,{\rm yr}^{-1}$, consistent with the value estimated by Cernicharo et al. (2010) of $\dot{M} = 4 \times 10^{-5}\,M_\odot\,{\rm yr}^{-1}$ ("with an uncertainty of a factor of $\simeq 2$") but with an expansion velocity of only $v_{\rm exp} = 5.8$ km s^{-1}, significantly slower than the observed expansion velocity of $v_{\rm exp}^{\rm obs} = 14.5$ km s^{-1} (Cernicharo et al. 2010). The gas–dust drift velocity reaches $v_{\rm D} = 10$ km s^{-1} in this model.

An AGB wind also forms when the luminosity is raised to $L = 18,000\,L_\odot$ (as is used by, e.g., Milam et al. 2009). We

calculated three models for differing effective temperatures ($T_{\rm eff} = 2100$, 2200, and 2300 K) and this luminosity, for which the expansion velocities are closer to the measured value, but which overestimates the mass-loss rate, especially at low stellar effective temperature (Table 5). The range of gas–dust drift velocities in these models is $8 \lesssim v_{\rm D} \lesssim 11$ km s^{-1}. Setting the luminosity to the intermediate values of $L = 10,000$ and $12,000\,L_\odot$ yields results intermediate between the higher and lower luminosities. None of the stellar parameter sets simultaneously yield both mass-loss rates and expansion velocities in agreement with observations. This will be further discussed in C. Sandin et al., (2022, in preparation). We note that the sound speed for all models, at the outer boundary, is $c_{\rm s} = 1.2$ km s^{-1}. Therefore, the ratio $v_{\rm D}/c_{\rm s} = 8.2$–$13 \gg 1.0$ implies a supersonic gas–dust interaction in the wind.

Table 5 shows the wind parameters for the models. The output parameters are the mass-loss rate ($\dot{M}$), the terminal
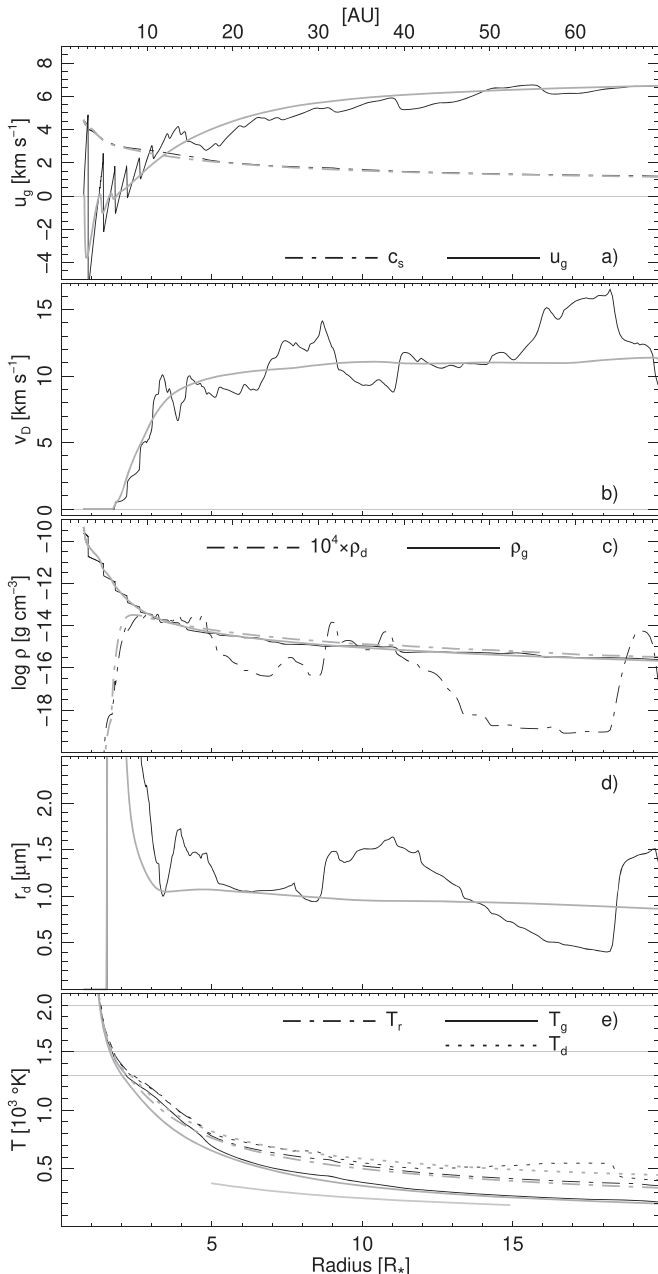
Figure 8. Radial plots of several wind parameters for our T-800 models, with $L_* = 10{,}000\,L_\odot$ and $T_{\rm eff} = 2100$ K. The five panels show, from top to bottom: (a) the (gas) expansion velocity ($u_{\rm g}$); (b) the gas–dust drift velocity ($v_{\rm D}$); (c) the gas and dust densities ($\rho_{\rm g}$ and $\rho_{\rm d}$); (d) the characteristic grain size ($r_{\rm d}$); and (e) the gas, dust, and radiative temperatures ($T_{\rm g}$, $T_{\rm d}$, and $T_{\rm r}$). Black lines show radial structures of a single snapshot. Gray lines show profiles averaged over multiple stellar pulsation periods. In the temperature plot (lowermost panel), the lower gray line shows $T \propto r^{-2/5}$.

expansion velocity of the wind ($v_{\rm exp}$), the gas–dust drift velocity ($v_{\rm D}$), the degree of condensation ($f_{\rm cond}$), the drift-dependent dust-to-gas mass-loss ratio ($\dot{M}_{\rm d}/\dot{M}$), and the grain size (radius; $r_{\rm d}$). The T-800 model does not generate a grain size distribution, but calculates the mean properties of the dust using moments of the grain size distribution.

Radial plots of the gas velocity, drift velocity, density structures, grain radius, and temperatures of the resulting stellar wind are shown in Figure 8. Notably, these new models reveal higher mass-loss rates than those discussed in Sandin & Mattsson (2020),

but the minimum drift velocity appears to be in line with the earlier results as it is about $10\,{\rm km\,s^{-1}}$.

5. Discussion

5.1. Temperature Modeling

As described in Section 3.3.2, while the overall shape of our modeled temperature profile should be reliable, since the CSE is optically thin at FIR wavelengths, the absolute temperature is less certain. To derive the correct scaling of the temperature profile, we would need to accurately determine the sublimation radius and, to less of an extent, the correct optical depth.

With this in mind, a detailed comparison between the absolute analytical temperature profile from Decin et al. (2011; derived from Decin et al. 2010), is not appropriate, but we can compare the relative profiles. As noted in Section 4.1, the profile from Decin et al. (2011) is steeper and produces a relatively lower temperature at larger radii than ours. This is due to differences in model assumptions. Decin et al. (2011) chose to ignore the inner region ($r < 15''$) of the CSE. Additionally, the shells derived, while in a similar location as ours, possess more total dust mass (indicated by the increased density contrasts in their study) than ours. This came about because the intensity profile is formed by the total optical depth along each sight line. Therefore, if a model does not allow for density enhancements within the inner region, this must be compensated for elsewhere. This increase in dust mass at larger radii then leads to a larger relative decrease in temperature.

We note that the dust temperature derived from a modified blackbody by Decin et al. (2011; Figure 6, data point) is much better aligned with our results than those from their analytical profile. This is most likely due to the fact that the derived grain composition in Decin et al. (2010) yields 72% amorphous carbon, 5% Fe, 13% SiC, and 10% MgS, while the temperature derived by Decin et al. (2011) assumes a CSE consisting solely of amorphous carbon. As noted in Section 5.1, the sublimation temperature, and thus the scaling of the temperature profile, is not only dependent on the sublimation radius but also on the grain chemistry in the CSE.

5.2. Grain Alignment

The striking characteristic of the polarization in the CSE of IRC+10° 216 is the centrosymmetric *radial* polarization pattern. Figure 9 shows a cartoon depicting grain alignment in IRC+10° 216. Girart et al. (2012) suggested that the magnetic field in the CSE might be generally radial (modulo the position angle uncertainty of Goldreich–Kulafis polarization), though this is put into question by the asymmetric results for the CN Zeeman measurements by Duthu et al. (2017). In addition, the small-scale structure of the source (e.g., Murakawa et al. 2005), indicating an obscuring torus and with possible outflow lobes, implies that the symmetry (likely rotation) axis of CW Leo is located close to the plane of the sky. In such a case no simple multipole magnetic field (except a monopole) would produce a radial magnetic geometry, unless the AGB wind dominates the magnetic forces and is dragging the magnetic field along in the outflow. Hence, irrespective of the grain mineralogy, magnetic alignment seems questionable. In comparison, SOFIA/HAWC+ observations of the oxygen-rich CSE around IK Tau can be well fitted by a projected dipole field (B.-G. Andersson et al. 2022, in preparation). Additionally, even if the wind is determining the geometry of the
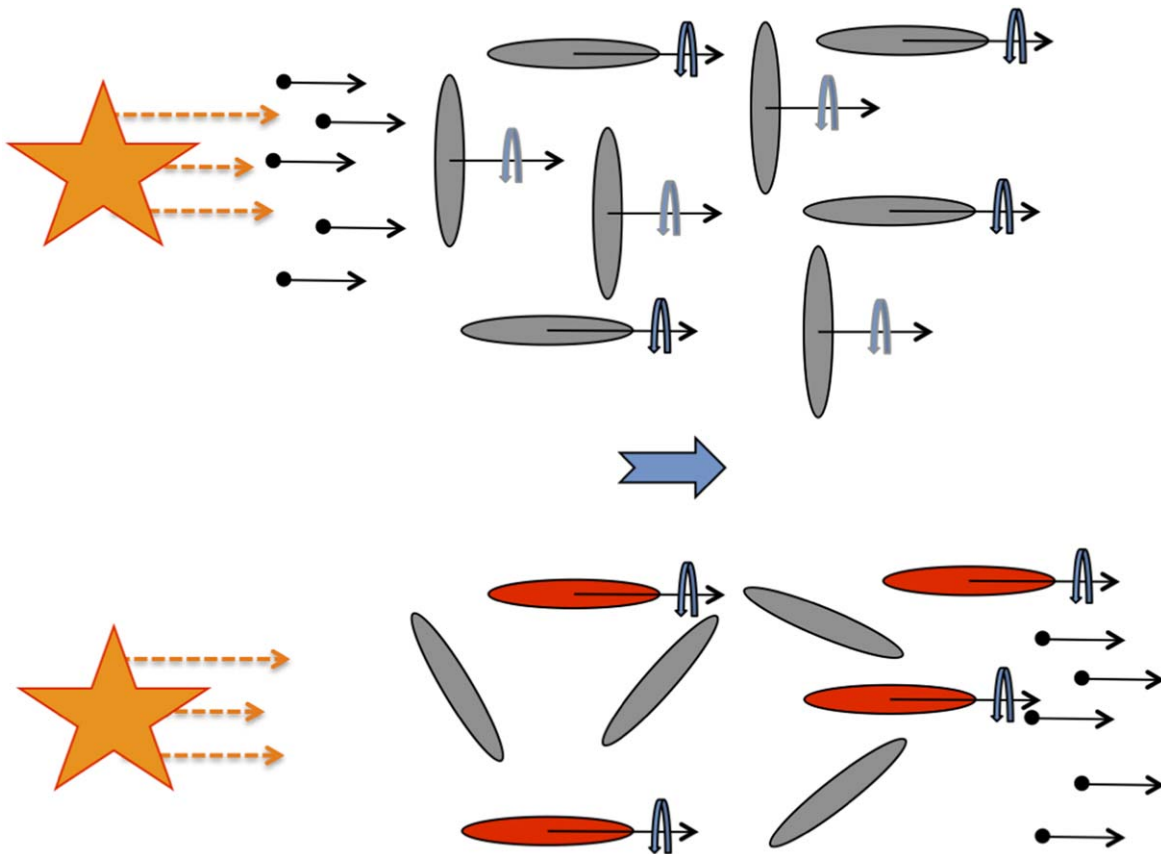
Figure 9. Cartoon of alignment in IRC+10° 216. Radiative alignment (k-RAT) on grains with weak, or no, internal alignment leads to grains being aligned both along and across the direction of the radiation field flow. The gas–dust drift means that the grains see a directed (supersonic) gas flow toward the star. This flow tends to randomize the grains with their short axes in the radiation field, and gas flow, direction, leaving the grains aligned with their short axes perpendicular to the radiation and gas flows. This generated a weak but systematic radial polarization in the CSE.

magnetic field, a radial polarization pattern is not consistent with magnetic alignment since in magnetically dominated alignment the long axis of the grains is expected to be oriented across the field lines. We therefore need to consider nonmagnetic grain-alignment mechanisms.

While RAT theory does provide for alignment along the radiation field direction for strong, anisotropic radiation fields ("k-RAT" alignment; Section 1), the expectation is, also for such alignment, that the grains are rotating with their minor axis around that reference direction, which should also yield an azimuthal FIR polarization pattern in an AGB envelope, at least for grains with efficient internal alignment. Hence, such first-order k-RAT is also not supported by the observations.

Given the expectation, supported by our modeling, that AGB star winds should have supersonic gas–dust drift velocities, other possibilities include "classical" Gold alignment and the MET mechanism proposed by Lazarian & Hoang (2007b; Section 1).

In "classical" mechanical (i.e., Gold) alignment the grains tumble in the gas flow—like water wheels in a stream—and align with their long axis in the direction of the flow, consistent with our observations. However, irregular grains in a gas–dust flow are expected to be aligned differently from the predictions of the classical Gold mechanism that assumes spheroidal grains. In the MET alignment mechanism (Lazarian & Hoang 2007b), irregular grains are preferentially aligned with long grain axes perpendicular to the flow, through physics analogous to the well-established RAT torques. The analytical

formulation of the MET alignment mechanism was recently tested in detailed numerical simulations by Hoang et al. (2018), who showed that it is more efficient than the alignment described by Gold (1952). This means that the latter mechanism is subdominant and realistic irregular grains align orthogonally to the Gold predictions in a gas–grain flow for both analytical and numerical calculations (ignoring radiative alignment). As for first-order k-RAT, the azimuthal polarization pattern predicted by MET alignment is inconsistent with our data.

Discussing mechanical alignment in shocks, Hoang & Lee (2020; their Equation (6)) show that the rms angular velocity of a grain experiencing a random-walk collision series achieves an average rotation speed of

$$\langle \omega^2 \rangle = \frac{(\Delta J)^2}{I^2} = \frac{n_H m_H^2 v_D^3 \pi a^4}{2I^2} \Delta t, \tag{5}$$
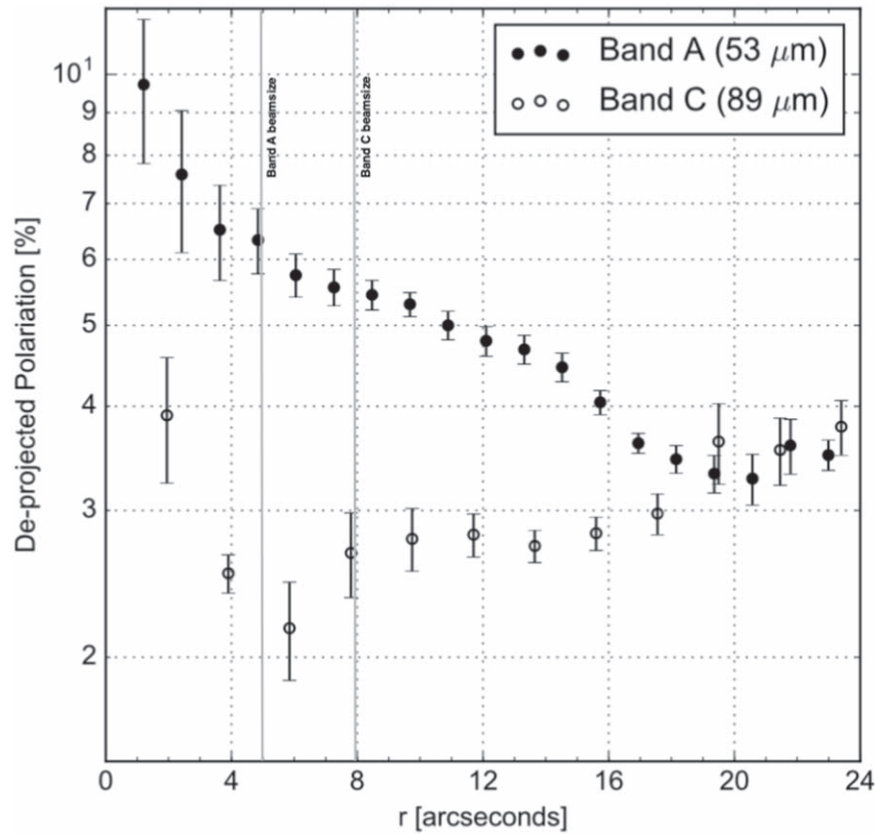
where I is the grain inertia moment.

The rotational damping due to the thermal evaporation of adsorbed H atoms yields a gas damping time, for $v_D \gg c_S$, of

$$\tau_H = \frac{3I}{2n_H m_H \pi a^4 v_D} \tag{6}$$

(see Equation(10) of Hoang & Lee 2020) and therefore

$$\langle \omega^2 \rangle = \frac{3m_H v_D^2}{4I}. \tag{7}$$

13

Figure 10. The radially averaged, deprojected, polarization for HAWC+ Band A (closed circles) and Band C (open circles). Only polarization measurements where $S/N \geqslant 5$ were considered. The beam sizes of bands A and C are indicated with gray lines.

Hence, for a supersonic drift velocity the collision-induced rotation speed (and hence alignment) is independent of the gas density. Since the drift speed, beyond a few tens of the stellar radius, is expected to be constant, so should the mechanical alignment. However, Figure 10 indicates that the alignment efficiency, as traced by the deprojected polarization, decreases with radius, providing additional evidence against mechanical alignment as the primary cause of the polarization in IRC+10° 216.

Finally we will consider a hybrid mechanism consisting of k-RAT alignment of grains without internal alignment (Hoang & Lazarian 2009) in a gas–dust flow combined with anisotropic collisional disalignment due to supersonic gas–dust flow.

The close correlation between the (deprojected) amount of polarization and the dust temperature indicate that the alignment should be radiation driven rather than—at least primarily—collisional.

A critical aspect in understanding the grain alignment in the CSE of IRC+10° 216 is the dust mineralogy. As noted above, the dust in this CSE is heavily dominated by amorphous carbon and SiC grains (Ivezić & Elitzur 1996a). Indirect evidence (Mauron & Huggins 2010) points to a minor component of solid iron, but it is not clear if such grains are separate or incorporated into composite dust. Carbonaceous solids are expected to be diamagnetic and therefore not subject to the Barnett effect or Barnett relaxation. We would, therefore, expect these grains to have—at best—poor internal alignment. As shown by Hoang & Lazarian (2009), grains with poor (or no) internal alignment can become aligned with the radiation field if it is strong and anisotropic enough. This alignment is inefficient and has two stable orientations relative to the

radiation k-vector, but in combination with the gas–dust drift in the CSE this would seem the best candidate to explain our observations. Figure 9 shows a cartoon depicting this grain-alignment mechanism. We are deferring a full ab initio modeling of the grain alignment in IRC+10° 216, based on RAT alignment, to a later paper, but discuss this preferred alignment mechanism here in a qualitative way.

Hoang & Lazarian (2009) explored RAT alignment for grains without internal alignment. They found that weak attractor points appear in the grain-alignment phase space under such conditions with (1) the minor grain axis oriented along the radiation field k-vector (as for grains with efficient internal alignment), and (2) with the major grain axis oriented along the reference direction.

As for all grain-alignment situations, in addition to the alignment-driving mechanism(s) the alignment-damping processes will also (potentially significantly) affect the observed polarization (Draine & Lazarian 1998; Soam et al. 2021). Because there is a significant supersonic gas–dust drift velocity in AGB star outflows (Section 4.3; Sandin & Mattsson 2020), collisional disalignment will likely be critical in these environments, and will tend to be anisotropic. For grains with a substantial axis ratio and an anisotropic orientation distribution (required to generate polarization) in a directional gas–dust flow, the collision rate will differ depending on the cross section of the grains to the gas flow. For the bimodal alignment distribution discussed by Hoang & Lazarian (2009), grains aligned "azimuthally" (with their long axis across the flow) will have a significantly larger cross section than those aligned "radially." Therefore, azimuthally aligned grains will be

randomized faster than those aligned radially. This would produce a net radial (FIR) polarization, as observed.

The most direct, testable consequence of this scenario is that, because of the weak attractor points for such k-RAT alignment, the fractional polarization should be low. In a forthcoming paper (B.-G. Andersson et al. 2022, in preparation) we show, based on optical spectropolarimetry of the background stars seen through the CSE of IRC+10° 216, that the fractional polarization from the dust in the CSE is only $p/A_V \simeq 0.7 \pm 0.2\%$ mag^{-1}, significantly lower than the ISM value of up to 4.2% mag^{-1} (Panopoulou et al. 2019), consistent with a poor alignment efficiency.

If the alignment is due to k-RAT alignment, and the polarization traces the full CSE, the alignment efficiency should be coupled with grain heating and hence grain temperature. From the results of the deprojected polarization scaling with the temperature (Figure 7), it is clear that this is the case for Band A.

The fitted scaling parameter for Band C indicates that there is formally a negative correlation between polarization and temperature and deprojected polarization. However, the deprojected polarization itself (Figure 10) shows that the polarization for Band C, outside the telescope beamwidth, is constant. The only increase in the polarization is at ∼18″, corresponding to the edge of the third shell (Table 4). While all the HAWC+ bands probe the emission well into the Rayleigh–Jeans tail of the blackbody emission of the denser CSE dust, Band C is at a longer wavelength than Band A and thus is less sensitive to the warm, well-aligned dust. Therefore the Band C polarization likely only traces the polarized emission for the colder dust further out in the CSE, and the emission may therefore be dominated by column density effects. As a result, the deprojected polarization in Band C is fairly constant. This is supported by the deprojected polarization for Band A, which toward the edge of the outermost shell also becomes nearly constant. Detailed modeling with radiative transfer codes, including the ability to incorporate k-RATs and carbonaceous dust in AGB wind structures, are needed to test these possibilities in detail. Such codes are now being completed and we expect to perform such quantitative polarization models in the near future.

6. Conclusions

We have used the HAWC+ instrument on SOFIA to map the polarization from the CSE of the carbon-rich AGB star IRC+10° 216. Using photometry and polarimetry from the HAWC+, along with archival photometry from Herschel/PACS, we model the temperature profile of the CSE. We find a centrosymmetric radial polarization pattern, unlikely to originate from dust aligned with the magnetic field. Because of the inherently radial nature of the implied grain alignment we deproject the polarization to the plane of the sky. This deprojected polarization, for HAWC+ Band A, (53 μm) is tightly correlated with the modeled temperature profile. For the longer-wavelength bands—specifically, Band C (89 μm)—the deprojected polarization is close to flat with distance from the central star. We argue, based on these results and supporting optical data, that the most likely grain-alignment mechanism active in the CSE of IRC+10° 216 is direct radiative alignment (so called "k-RAT" alignment) on grains with poor internal alignment, combined with anisotropic collisional disalignment caused by the gas–dust drift inherent in AGB winds. The

required grain characteristic is a natural consequence of the diamagnetic nature of carbon dust. We show, using state-of-the-art simulations, that the drift velocity in the IRC+10° 216 wind is likely of the order of 10 km s^{-1}. The poor alignment efficiency implied by optical polarimetry observations, the tight polarization–grain temperature correlation, as well as theoretical efficiency considerations make it unlikely that the implied grain alignment is caused by classical mechanical (i.e., "Gold") alignment. New, more realistic modeling codes including the evolving physics of grain alignment will be used to test these conclusions in the near future.

Appendix A
Differential Evolution Minimization

Differential evolution operates by first evaluating a random population of trial solutions within user-defined parameter bounds. The value of each trial solution is referred to as its fitness and is what is being minimized. This step is referred to as initialization, and the candidates in this population belong to generation (G) zero. This is followed by a mutation stage where, for a given candidate, $x_{i,G}$, three additional random candidates are chosen ($x_{r1,G}$, $x_{r2,G}$, and $x_{r3,G}$), where i, $r1$, $r2$, and $r3$ are unique indices. A donor candidate, $v_{i,G+1}$, is then created by

$$v_{i,G+1} = x_{r1,G} + F(x_{r2,G} - x_{r3,G}). \tag{A1}$$

Here, F is a mutation factor, which is user specified and where $0 \leqslant F \leqslant 2$.

Then begins the next evolutionary stage, recombination. This stage attempts to incorporate successful solutions from the previous generation by developing future candidates with elements from a given candidate and its corresponding donor candidate in order to create a trial candidate, $u_{i,G+1}$, based on the following:

$$u_{j,i,G+1} = \begin{cases} v_{j,i,G+1} & \text{if } \mathrm{rand}_{j,i} \leqslant CR \text{ or } j = j_{\mathrm{rand}} \\ x_{j,i,G} & \text{if } \mathrm{rand}_{j,i} > CR \text{ and } j \neq j_{\mathrm{rand}} \end{cases}. \tag{A2}$$

In this scheme, j refers to some parameter for the given candidate, $\mathrm{rand}_{j,i}$ is a random value between zero and one, and CR is the user-specified recombination rate, where $0 \leqslant CR \leqslant 1$. The use of j_{rand} in the "or" statement ensures that $u_{i,G+1} \neq x_{i,G}$.
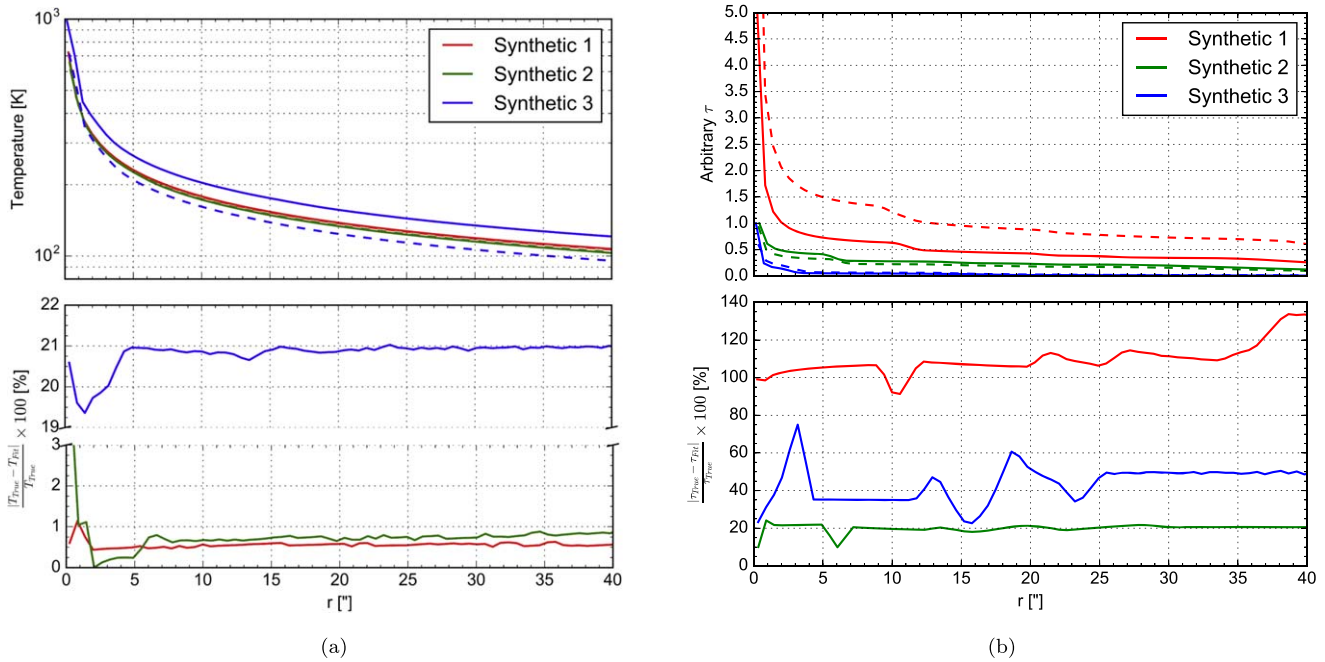
Figure 11. Upper panel (a): DUSTY-modeled temperature as a function of radius from the central source for the synthetic data set (solid lines) and the result of the differential evolution fitting (dashed lines) for each synthetic data set. Lower panel (a): percent difference between the temperatures profile for the synthetic data and the fitted data. Upper panel (b): DUSTY-modeled relative optical depth as a function of radius from the central source for the synthetic data set (solid lines) and the result of the differential evolution fitting (dashed lines) for each synthetic data set. The optical depth scale is arbitrary and true peaks in optical depth are reflected by total optical depth values in Table 6. Lower panel (b): percent difference between the relative optical depth profile for the synthetic data and the fitted data.

Finally, the candidates for the next generation are selected, wherein only the best candidates are chosen, or

$$x_{i,G+1} = \begin{cases} u_{i,G+1} & \text{if } f(u_{i,G+1}) \leqslant f(x_{i,G}) \\ x_{i,G} & \text{if } f(u_{i,G+1}) > f(x_{i,G}). \end{cases} \quad (A3)$$

Because of this selection criterion, the fitness of the candidates either remains the same or improves throughout the generations.

This process of mutation, recombination, and selection is then repeated until the maximum number of generations are reached, or when the standard deviation in fitness values for a given generation falls below a user-defined threshold. Following the elimination of such a routine, it is common practice to use the result as the starting point for a least-squares optimization to "polish" the final result. It should be noted that there is no proof of convergence for differential evolution minimization.

The setting of the differential evolution parameters F and CR was based on the study of high-dimensional optimization problems by Kukkonen & Lampinen (2006). Kukkonen & Lampinen (2006) found that for such problems

$$c = \sqrt{2F^2 CR - \frac{2CR}{N} + \frac{CR^2}{N} + 1}, \quad (A4)$$

where for $c < 1$ the recombination and mutation operations decrease the population variance, for $c = 1$ the variance does not change, and for $c > 1$ the variance increases. As differential evolution naturally decreases the variance, a $c > 1$ would be necessary to prevent a premature convergence with a narrow search coverage, and generally $1 < c < 1.5$ is recommended. In order to achieve this, it should be noted that we are not using a fixed mutation factor, but instead will allow the mutation scaling factor to vary randomly between some bounded region between generations. As an increase in the mutation rate increases the search area, and we will be using a scheme to initialize the population that covers a large area (latin hypercube sampling), we will use a slightly lower mutation rate in order for each candidate to do a more local search in its region of dimensional space. Thus, we decided to use a varying mutation factor, where the factor changes randomly between 0.4 and 0.6, and a recombination rate of 0.8 (which corresponds to $c \sim 1.2$).

Using the relationships described above, we can begin to understand the errors found in the fits to the synthetic data in Appendix B. First, we will consider the fitted optical depth profiles (Figure 11(a)). We find that the fitting procedure is able to determine the relative shape of the optical depth profile outside of the shell thicknesses. This is due to the fact that, with the resolution of our images, we are not able to resolve these shells, so according to the reasoning above we should not be capable of determining the optical depth along these sight lines. Then, the reason why we are not able to correctly determine the absolute optical optical depth profile (i.e., the overall optical depth) is due to the fact that we are only considering the fit to the normalized intensity profile, and thus are not considering the peak in the absolute intensity. Second, as stated above, we are not able to deduce the sublimation radius with our data given our resolution and wavelength range. So, it is not surprising that we are not capable of doing this in all cases for the synthetic data fits. These discrepancies in sublimation radius and overall optical depth manifest in a change in sublimation temperature (per Equation (2)) that then accounts for the scaled differences in the temperature profile.

Table 6
Fitted Parameters for Our Synthetic Data Using a Least-squares Optimization with the Result of the Differential Evolution as the Starting Point and a Least-squares Optimization

Parameter	Units	Synthetic 1 (S1)		Synthetic 2 (S2)		Synthetic 3 (S3)	
		True Values	DE Fit + LS	True Values	DE Fit + LS	True Values	DE Fit + LS
τ_{λ_0}	⋯	2.6×10^{-4}	5.19×10^{-4}	1×10^{-3}	9.47×10^{-4}	0.02	.0121
$C_{s,1}$	⋯	10	6.00	15	16.0	5	5.04
$C_{is,2}$	⋯	2	2.33	1	0.616	0.5	0.557
$C_{s,2}$	⋯	10	8.32	10	6.79	8	11.2
$C_{is,3}$	⋯	2	3.89	4	5.76	3	7.11
$C_{s,3}$	⋯	10	4.01	12	8.21	15	10.3
$C_{is,4}$	⋯	2	3.31	1	4.77	1	3.63
$C_{s,4}$	⋯	10	7.31	18	18.7	9	12.4
C_{os}	⋯	1×10^{-3}	1.16×10^{-3}	5×10^{-3}	3.16×10^{-3}	1×10^{-4}	5.19×10^{-4}
r_{sub}	″	0.25	0.247	0.4	0.324	0.15	0.312
r_1	″	10	8.97	5.4	6.02	2.15	2.46
t_1	″	2	3.02	1	0.846	1	1.49
r_2	″	20	20.3	13.4	12.7	12.15	13.0
t_2	″	2	1.87	2	2.11	0.5	3.66
r_3	″	25	24.8	19.4	16.8	15.65	18.2
t_3	″	2	4.85	3	4.56	3	1.54
r_4	″	34	34.8	27.4	27.3	22.65	22.5
t_4	″	2	3.34	1	2.71	2.5	0.871
L_{st} [a]	$L_\odot$	5258	5258	5258	5258	5258	5258
T_{st} [a]	K	2200	2200	2200	2200	2200	2200

Note. The description for the parameters above are shown in Table 4.
[a] Fixed parameters.

Appendix B
Synthetic Data

In this appendix, we describe the creation of and results from synthetic data fits using the optimization procedure described in Section 3.3.2. We have created three synthetic data sets, and in order to make these data sets as close to our true data, we have used the same model as we assume explains the dust distribution around IRC+10°216 (Section 3.3.1), and chose parameters within the search grid we used for the differential evolution fit to the observed data. We then created images at the five wavelengths of our images using DUSTY and convolved these images using the kernels in Table 3. At this point, we did want to add some noise to the images that is comparable to the noise present in our images. To do this, we looked at the average S/N (based on the distance from the center of the image) for each image and applied a random amount of noise, with the average level of noise of a bin being the max allowed, to our synthetic images. For the three synthetic data sets we ensured that each set of parameters were in a different optical depth regime, had a different dust distribution and had a different sublimation radius (and thus sublimation temperature). The resulting optimized parameters for each synthetic data set using the same fitting scheme and differential evolution parameters as described in Section 3.3.2 are shown in Table 6.

We also extracted the temperature (Figure 11(a)) and optical depth (Figure 11(b)) profiles for the synthetic data sets and the resulting fits. For all data sets, we find large discrepancies in the optical depth profiles, which, depending on the total optical depth, may manifest in large absolute changes in temperature. All changes in temperature profile that manifest from these errors, though, seem to be constant outside of the smallest beam, indicating the resulting shape of the fitted temperature profiles is correct.

ORCID iDs

B-G Andersson ⓘ https://orcid.org/0000-0001-6717-0686
Enrique Lopez-Rodriguez ⓘ https://orcid.org/0000-0001-5357-6538
Ilija Medan ⓘ https://orcid.org/0000-0003-3410-5794
Archana Soam ⓘ https://orcid.org/0000-0002-6386-2906
Thiem Hoang ⓘ https://orcid.org/0000-0003-2017-0982
John E. Vaillancourt ⓘ https://orcid.org/0000-0001-8916-1828
Alex Lazarian ⓘ https://orcid.org/0000-0002-7336-6674
Christer Sandin ⓘ https://orcid.org/0000-0002-6370-5505
Lars Mattsson ⓘ https://orcid.org/0000-0003-2670-2513
Mehrnoosh Tahani ⓘ https://orcid.org/0000-0001-8749-1436

References

Abbas, M. M., Tankosic, D., Craven, P. D., et al. 2006, ApJ, 645, 324
Agúndez, M., Fonfría, J. P., Cernicharo, J., et al. 2012, A&A, 543, A48
Andersson, B.-G., Lazarian, A., & Vaillancourt, J. E. 2015, ARA&A, 53, 501
Becklin, E. E., Frogel, J. A., Hyland, A. R., Kristian, J., & Neugebauer, G. 1969, ApJL, 158, L133
Bergeat, J., Knapik, A., & Rutily, B. 2001, A&A, 369, 178
Bocchio, M., Bianchi, S., & Abergel, A. 2016, A&A, 591, A117
Canovas, H., Ménard, F., de Boer, J., et al. 2015, A&A, 582, L7
Cernicharo, J., Waters, L. B. F. M., Decin, L., et al. 2010, A&A, 521, L8
Chandrasekhar, S., & Fermi, E. 1953, ApJ, 118, 113
Chiar, J. E., Adamson, A. J., Whittet, D. C. B., et al. 2006, ApJ, 651, 268
Chiar, J. E., Tielens, A. G. G. M., Adamson, A. J., & Ricca, A. 2013, ApJ, 770, 78
Chuss, D. T., Andersson, B. G., Bally, J., et al. 2019, ApJ, 872, 187
Cohen, M. 1979, MNRAS, 186, 837
Cudlip, W., Furniss, I., King, K. J., & Jennings, R. E. 1982, MNRAS, 200, 1169
Davis, L. 1951, PhRv, 81, 890
Davis, L. J., & Greenstein, J. L. 1951, ApJ, 114, 206
De Beck, E., Lombaert, R., Agúndez, M., et al. 2012, A&A, 539, A108
Decin, L., Agúndez, M., Barlow, M. J., et al. 2010, Natur, 467, 64
Decin, L., Royer, P., Cox, N. L. J., et al. 2011, A&A, 534, A1

Dolginov, A. Z., & Mitrofanov, I. G. 1976, Ap&SS, 43, 291
Dowell, C. D., Cook, B. T., Harper, D. A., et al. 2010, Proc. SPIE, 7735, 77356H
Draine, B. T., & Fraisse, A. A. 2009, ApJ, 696, 1
Draine, B. T., & Hensley, B. S. 2021, ApJ, 909, 95
Draine, B. T., & Lazarian, A. 1998, ApJ, 508, 157
Draine, B. T., & Weingartner, J. C. 1996, ApJ, 470, 551
Duthu, A., Herpin, F., Wiesemeyer, H., et al. 2017, A&A, 604, A12
Einstein, A., & de Haas, W. J. 1915, KNAB, 18, 696
Fox-Middleton, S., Soam, A., Andersson, B., & Kulas, K. 2021, AAS Meeting, 53, 130.04
Gail, H.-P., & Sedlmayr, E. 2013, Physics and Chemistry of Circumstellar Dust Shells (Cambridge: Cambridge Univ. Press)
Gandilo, N. N., Ade, P. A. R., Angilè, F. E., et al. 2016, ApJ, 824, 84
Gehrz, R. D., Evans, A., Woodward, C. E., et al. 2018, ApJ, 858, 78
Girart, J. M., Patel, N., Vlemmings, W. H. T., & Rao, R. 2012, ApJL, 751, L20
Gold, T. 1952, MNRAS, 112, 215
Groenewegen, M. A. T., Barlow, M. J., Blommaert, J. A. D. L., et al. 2012, A&A, 543, L8
Guelin, M., Forestini, M., Valiron, P., et al. 1995, A&A, 297, 183
Guzman-Ramirez, L., Lagadec, E., Wesson, R., et al. 2015, MNRAS, 451, L1
Habing, H. J., Tignon, J., & Tielens, A. G. G. M. 1994, A&A, 286, 523
Hall, J. S. 1949, Sci, 109, 166
Hanner, M. 1988, Grain optical properties, Tech. Rep, SEE N89-13330 04-89, NASA
Harper, D. A., Runyan, M. C., Dowell, C. D., et al. 2018, JAI, 7, 1840008
Hensley, B. S., & Draine, B. T. 2021, ApJ, 906, 73
Heremans, J., Olk, C. H., & Morelli, D. T. 1994, PhRvB, 49, 15122
Hiltner, W. A. 1949a, ApJ, 109, 471
Hiltner, W. A. 1949b, Sci, 109, 165
Hoang, T., Cho, J., & Lazarian, A. 2018, ApJ, 852, 129
Hoang, T., & Lazarian, A. 2009, ApJ, 697, 1316
Hoang, T., Lazarian, A., & Martin, P. G. 2014, ApJ, 790, 6
Hoang, T., & Lee, H. 2020, ApJ, 896, 144
Houde, M., Vaillancourt, J. E., Hildebrand, R. H., Chitsazzadeh, S., & Kirby, L. 2009, ApJ, 706, 1504
Hough, J. H., Aitken, D. K., Whittet, D. C. B., Adamson, A. J., & Chrysostomou, A. 2008, MNRAS, 387, 797
Hu, C.-Y., Zhukovska, S., Somerville, R. S., & Naab, T. 2019, MNRAS, 487, 3252
Ivezić, Z., & Elitzur, M. 1996a, MNRAS, 279, 1019
Ivezić, Z., & Elitzur, M. 1996b, MNRAS, 279, 1011
Ivezić, Z., & Elitzur, M. 1997, MNRAS, 287, 799
Jones, R. V., & Spitzer, L., Jr. 1967, ApJ, 147, 943
Jones, T. J., Hyland, A. R., & Bailey, J. 1984, ApJ, 282, 675
Jura, M. 1994, ApJ, 434, 713
Kataoka, A., Tsukagoshi, T., Pohl, A., et al. 2017, ApJ, 844, L5
Kim, S.-H., & Martin, P. G. 1994, ApJ, 431, 783
Kovács, A. 2006, PhD thesis, Caltech
Kovács, A. 2008, Proc. SPIE, 7020, 70201S
Kukkonen, S., & Lampinen, J. 2006, in 2006 IEEE Int. Conf. on Evolutionary Computation (Piscataway, NJ: IEEE), 207
Kwan, J., & Hill, F. 1977, ApJ, 215, 781
Ladjal, D., Barlow, M. J., Groenewegen, M. A. T., et al. 2010, A&A, 518, L141
Lattanzio, J. C., & Wood, P. R. 2004, in Evolution, Nucleosynthesis, and Pulsation of AGB Stars, ed. H. J. Habing & H. Olofsson, Vol. 23 (Berlin: Springer)
Lazarian, A. 1994, MNRAS, 268, 713

Lazarian, A. 1995a, MNRAS, 277, 1235
Lazarian, A. 1995b, ApJ, 451, 660
Lazarian, A. 2020, ApJ, 902, 97
Lazarian, A., & Draine, B. T. 1999a, ApJL, 520, L67
Lazarian, A., & Draine, B. T. 1999b, ApJL, 516, L37
Lazarian, A., & Efroimsky, M. 1996, ApJ, 466, 274
Lazarian, A., & Efroimsky, M. 1999, MNRAS, 303, 673
Lazarian, A., Efroimsky, M., & Ozik, J. 1996, ApJ, 472, 240
Lazarian, A., & Hoang, T. 2007a, MNRAS, 378, 910
Lazarian, A., & Hoang, T. 2007b, ApJL, 669, L77
Lazarian, A., & Hoang, T. 2019, ApJ, 883, 122
Liu, L., Lu, F., Tian, J., Xia, S., & Diao, Y. 2019, ApPhA, 125, 366
Lopez-Rodriguez, E., Fuller, L., Alonso-Herrero, A., et al. 2018, ApJ, 859, 99
Mathis, J. S. 1986, ApJ, 308, 281
Mathis, J. S., Rumpl, W., & Nordsieck, K. H. 1977, ApJ, 217, 425
Mauron, N., & Huggins, P. J. 1999, A&A, 349, 203
Mauron, N., & Huggins, P. J. 2000, A&A, 359, 707
Mauron, N., & Huggins, P. J. 2010, A&A, 513, A31
Medan, I., & Andersson, B.-G. 2019, ApJ, 873, 87
Menten, K. M., Reid, M. J., Kamiński, T., & Claussen, M. J. 2012, A&A, 543, A73
Milam, S. N., Woolf, N. J., & Ziurys, L. M. 2009, ApJ, 690, 837
Miller, J. S. 1970, ApJL, 161, L95
Murakawa, K., Suto, H., Oya, S., et al. 2005, A&A, 436, 601
Olofsson, H. 2004, Circumstellar Envelopes, Vol. 325 (Berlin: Springer)
Panopoulou, G. V., Hensley, B. S., Skalidis, R., Blinov, D., & Tassis, K. 2019, A&A, 624, L8
Pattle, K., Lai, S.-P., Wright, M., et al. 2021, MNRAS, 503, 3414
Pegourie, B. 1988, A&A, 194, 335
Pelletier, J., Gervais, D., & Pomot, C. 1984, JAP, 55, 994
Phillips, J. P., White, G. J., Ade, P. A. R., et al. 1982, A&A, 116, 130
Purcell, E. M. 1979, ApJ, 231, 404
Ramstedt, S., Schöier, F. L., Olofsson, H., & Lundgren, A. A. 2008, A&A, 487, 645
Richardson, O. W. 1908, PhRvI, 26, 248
Ridgway, S., & Keady, J. J. 1988, ApJ, 326, 843
Sahai, R., & Chronopoulos, C. K. 2010, ApJL, 711, L53
Sandin, C. 2008, MNRAS, 385, 215
Sandin, C., & Mattsson, L. 2020, MNRAS, 499, 1531
Santos, F. P., Chuss, D. T., Dowell, C. D., et al. 2019, ApJ, 882, 113
Schmid, H. M., Joos, F., & Tschan, D. 2006, A&A, 452, 657
Smith, C. H., Wright, C. M., Aitken, D. K., Roche, P. F., & Hough, J. H. 2000, MNRAS, 312, 327
Soam, A., Andersson, B.-G., Acosta-Pulido, J., et al. 2021, ApJ, 907, 93
Soam, A., Andersson, B. G., Straižys, V., et al. 2021, AJ, 161, 149
Storn, R., & Price, K. 1997, J. Glob. Optim., 11, 341
Tuthill, P. G., Monnier, J. D., Danchi, W. C., & Lopez, B. 2000, ApJ, 543, 284
Vaillancourt, J. E., Chuss, D. T., Crutcher, R. M., et al. 2007, Proc. SPIE, 6678, 66780D
Vaillancourt, J. E., Dowell, C. D., Hildebrand, R. H., et al. 2008, ApJL, 679, L25
Voshchinnikov, N. V., Henning, T., Prokopjeva, M. S., & Das, H. K. 2012, A&A, 541, A52
Wang, Y., Liu, Y., Wang, G., et al. 2015, NatSR, 5, 8999
Weigelt, G., Balega, Y., Bloecker, T., et al. 1998, A&A, 333, L51
Whittet, D. C. B. 2003, Dust in the Galactic Environment (2nd edn.; Bristol: IOP Publishing), 390
Woodward, C. E., Evans, A., Banerjee, D. P. K., et al. 2021, AJ, 162, 183